Ca^{2+}-saturated calmodulin binds tightly to the N-terminal domain of A-type fibroblast growth factor homologous factors

Received for publication, December 17, 2020, and in revised form, February 15, 2021 Published, Papers in Press, February 24, 2021,
https://doi.org/10.1016/j.jbc.2021.100458

Ryan Mahling, Cade R. Rahlf, Samuel C. Hansen, Matthew R. Hayden, and Madeline A. Shea*
From the Department of Biochemistry, Carver College of Medicine, University of Iowa, Iowa City, Iowa, USA

Edited by Karen Fleming

Voltage-gated sodium channels (Na_vs) are tightly regulated by multiple conserved auxiliary proteins, including the four fibroblast growth factor homologous factors (FGFs), which bind the Na_v EF-hand like domain (EFL), and calmodulin (CaM), a multifunctional messenger protein that binds the Na_V IQ motif. The EFL domain and IQ motif are contiguous regions of Na_V cytosolic C-terminal domains (CTD), placing CaM and FGF in close proximity. However, whether the FGFs and CaM act independently, directly associate, or operate through allosteric interactions to regulate channel function is unknown. Titrations monitored by steady-state fluorescence spectroscopy, structural studies with solution NMR, and computational modeling demonstrated for the first time that both domains of $(Ca^{2+})_4$-CaM (but not apo CaM) directly bind two sites in the N-terminal domain (NTD) of A-type FGF splice variants (FGF11A, FGF12A, FGF13A, and FGF14A) with high affinity. The weaker of the $(Ca^{2+})_4$-CaM-binding sites was known *via* electrophysiology to have a role in long-term inactivation of the channel but not known to bind CaM. FGF12A binding to a complex of CaM associated with a fragment of the $Na_V1.2$ CTD increased the Ca^{2+}-binding affinity of both CaM domains, consistent with $(Ca^{2+})_4$-CaM interacting preferentially with its higher-affinity site in the FGF12A NTD. Thus, A-type FGFs can compete with Na_V IQ motifs for $(Ca^{2+})_4$-CaM. During spikes in the cytosolic Ca^{2+} concentration that accompany an action potential, CaM may translocate from the Na_V IQ motif to the FGF NTD, or the A-type FGF NTD may recruit a second molecule of CaM to the channel.

The human voltage-gated sodium channels (Na_V) are a family of nine proteins ($Na_V1.1$–$Na_V1.9$) that are responsible for the generation and propagation of action potentials in excitable tissues throughout the human body. The functional core of each Na_V is a single transmembrane pore-forming α-subunit that interacts with one or more auxiliary β-subunits (Fig. 1, *A* and *B*) (1). The physiological function of Na_Vs requires the α-subunit to rapidly transition among closed, opened, and inactivated states. The importance of rapidly cycling among these functional states is highlighted by the identification of disease-causing mutations throughout the sequences of the Na_V isoforms that disrupt this process to cause debilitating conditions including epileptic disorders (2–6), cardiomyopathies (7–10), and chronic pain (11–13).

The transition of an Na_V α-subunit among its functional states is tightly regulated by a network of protein–protein interactions. These include intramolecular interactions among cytosolic regions of the α-subunit including the inactivation gate and intermolecular interactions between the cytosolic N-terminal (NTD) and C-terminal domains (CTD) of the channel and several auxiliary proteins (14–16). The Na_V CTD interacts with multiple auxiliary proteins including fibroblast growth factor homologous factors (FGFs or FHFs) that bind to an acidic EF-hand-like domain (EFL) (17–21) and the ubiquitously expressed and essential Ca^{2+} sensor calmodulin (CaM) that binds to a highly conserved basic IQ motif (IQxxx[R,K]Gxxx[R,K]) (Fig. 1*B*) (22–28).

CaM is composed of two four-helix bundle domains (CaM_N and CaM_C). They are connected by a flexible linker that allows the domains to move independently in solution. Both CaM_N and CaM_C contain a pair of EF-hands that bind Ca^{2+} cooperatively. In free CaM, CaM_C has an affinity for Ca^{2+} that is approximately tenfold higher than that of CaM_N (29–31) resulting in sequential occupancy of the domains. In eukaryotes, CaM regulates many proteins in a Ca^{2+}-dependent manner (32–36). Binding these targets selectively increases or decreases the Ca^{2+}-binding affinity of one or both domains of CaM, making CaM an effective Ca^{2+} sensor over a wide range (10^3) of Ca^{2+} concentrations (37).

Ca^{2+}-depleted (apo) CaM and $(Ca^{2+})_4$-CaM bind tightly to many IQ motifs. These basic amphipathic α-helix (BAA) CaM binding domains (CaMBDs) are found in all human Na_V isoforms, and CaM–Na_V interactions have been especially well studied in $Na_V1.2$ and $Na_V1.5$ (23–27). Despite both apo and $(Ca^{2+})_4$-CaM having a high affinity for these IQ motifs, how CaM acts as a Ca^{2+} sensor to modulate Na_V function is poorly understood. Ca^{2+} binding to CaM_C induces a ∼180° rotation of CaM_C on the $Na_V1.2$ IQ motif (25). This rotation may require transient release and reassociation of CaM_C with the IQ motif, which could also allow CaM to translocate to a different high-affinity CaMBD.

* For correspondence: Madeline A. Shea, madeline-shea@uiowa.edu.

The four FGF isoforms (FGF11–FGF14) that bind the EFL domain of Na_Vs are a subgroup of the fibroblast growth factor superfamily (38). Crystallographic structures (39, 40) showed that they contain a well-folded β-trefoil core that is nearly identical to that of canonical fibroblast growth factors (41). However, unlike most members of the FGF family, these FGFs are not secreted (38, 42). Rather, they remain in the cytosol and have been implicated in trafficking and modulating Na_V channel properties including persistent current (17, 19, 21, 43, 44).

Multiple splice variants have been identified for each of the four FGF isoforms (Fig. 1*C*). These arise primarily from differential splicing of the first exon and result in sequences that vary in the length and composition of the NTD (42, 45). The effect of FGFs on Na_V function depends on the splice variant bound (21, 43, 46, 47). The B-type splice variants typically have a shorter NTD and are associated with changing current density. The A-type splice variants typically have a longer NTD and are specifically associated with an increased rate of inactivation and long-term inactivation of the Na_V α-subunit, which has been proposed to result from an interaction between a region in the NTD and the channel (43). The differences suggest important roles for the distinct NTD sequence of each FGF splice variant.

Colocalization experiments have found that CaM and the FGFs interact with multiple Na_V isoforms within cells (47–50). Proteomics studies have shown that CaM and FGF12 interact with $Na_V1.2$ in neurons (16). Crystallographic structures of a B-type FGF (FGF12B and FGF13U) and CaM bound to Na_V CTD fragments that contain both the EFL and IQ motif (26, 51) showed that CaM and FGFs are bound near each other. Recently, an indirect allosteric interaction has been proposed to occur between CaM and FGF12B on $Na_V1.4$ (52). However, there has been no evidence supporting CaM directly binding any splice variant of an FGF isoform.

Here we report for the first time that CaM binds the NTD of each A-type FGF (FGF11A, FGF12A, FGF13A, and FGF14A) in a Ca^{2+}-dependent manner. Using steady-state fluorescence spectroscopy, copurification, and solution NMR, we show that CaM binds two sequences in the NTD of each A-type FGF with high affinity and that both domains of $(Ca^{2+})_4$-CaM mediate this interaction. Focusing on FGF12 because of the cellular and structural studies cited above, we demonstrate that binding of full-length FGF12A to a fragment of the $Na_V1.2$ CTD ($Na_V1.2_{CTD}$, residues 1777–1937) containing the EFL and IQ motif increases the Ca^{2+} affinity of both CaM domains. Because the IQ motif is known to lower Ca^{2+} affinity of CaM_C, this new finding is consistent with $(Ca^{2+})_4$-CaM interacting favorably with the NTD of FGF12A in this ternary complex. These results support a model in which the A-type FGFs compete with Na_V IQ motifs for $(Ca^{2+})_4$-CaM and suggest that, during spikes in the local cytosolic Ca^{2+} concentration, CaM may translocate from an Na_V IQ motif to an A-type FGF NTD or that the NTD may recruit an additional CaM molecule to the ternary complex.

Results

Potential CaM-binding sites in NTDs of A-type FGFs

CaM is known to bind tightly to sequences that are intrinsically disordered but that adopt helical geometry when bound by CaM. The NTD sequences of A-type splice variants of intracellular FGFs are thought to be disordered. However, an analysis of the FGF11A, FGF12A, FGF13A, and FGF14A sequences with the Protein Disorder Prediction System (53) showed two minima in the NTD of each FGF isoform (Fig. 1, *C* and *D*) suggesting that two segments are capable of adopting ordered secondary structure and might be CaM-binding sites.

One sequence is near the N terminus of the NTD (referred to as the long-term inactivation particle or LTP). It is highly conserved among the four human FGF isoforms (Fig. 1*E*) and across species (Fig. S1, *A–D*, Table S1–S4) and was shown to contribute functionally to long-term inactivation of Na_Vs mediated by A-type FGFs (43). The other sequence is C terminal to the LTP (referred to hereafter as the CaM-binding domain (CaMBD)). Although the CaMBD has a more variable sequence among the four human FGF isoforms (Fig. 1*F*), the CaMBD sequence of each isoform is highly conserved across species (Fig. S1, *E–H*, Table S5–S8). Currently it has no known function.

To explore whether the FGF LTP and CaMBD regions might function as CaM-binding sites, α-helical models were made with PyMOL and helical wheels were generated based on the sequence of the FGF12A LTP and CaMBD (Fig. S2, *A–F*). The sequences each contained an aliphatic patch bracketed by basic residues consistent with other BAA motifs that are known to bind tightly to CaM.

To understand whether these putative sites in the FGF NTD would be accessible to CaM, it would be helpful to have an experimentally determined structure; however, none are available for any of the full-length A-type FGFs. Therefore, structural models of full-length FGF12A were generated with Robetta (54). Each model in the ensemble had a well-folded β-trefoil core that was nearly identical to that of a crystallographically determined structure of FGF12B (Fig. S3, *A* and *B*) (39). New insights came from modeling of the FGF12A NTD that included the LTP and CaMBD. Both potential CaM-binding sites were predicted to adopt α-helical secondary structure (Fig. S3*B*). They were connected by a disordered linker (aa 18–39), and the CaMBD region was connected to the β-trefoil core by another disordered linker (aa 52–69). These linkers would allow the LTP and CaMBD to sample many orientations relative to each other and relative to the β-trefoil core as shown in the set of five lowest-energy (most favorable) conformations (Fig. S3, *C–H*). The predicted secondary structure and BAA motif sequences of the FGF12A LTP and CaMBD suggested that both were strong candidates for CaM binding.

$(Ca^{2+})_4$-saturated CaM tightly binds two sites in the A-type FGFs

To determine whether CaM binds the FGF LTP or CaMBD, apo or $(Ca^{2+})_4$-CaM was added to biosensors in which the

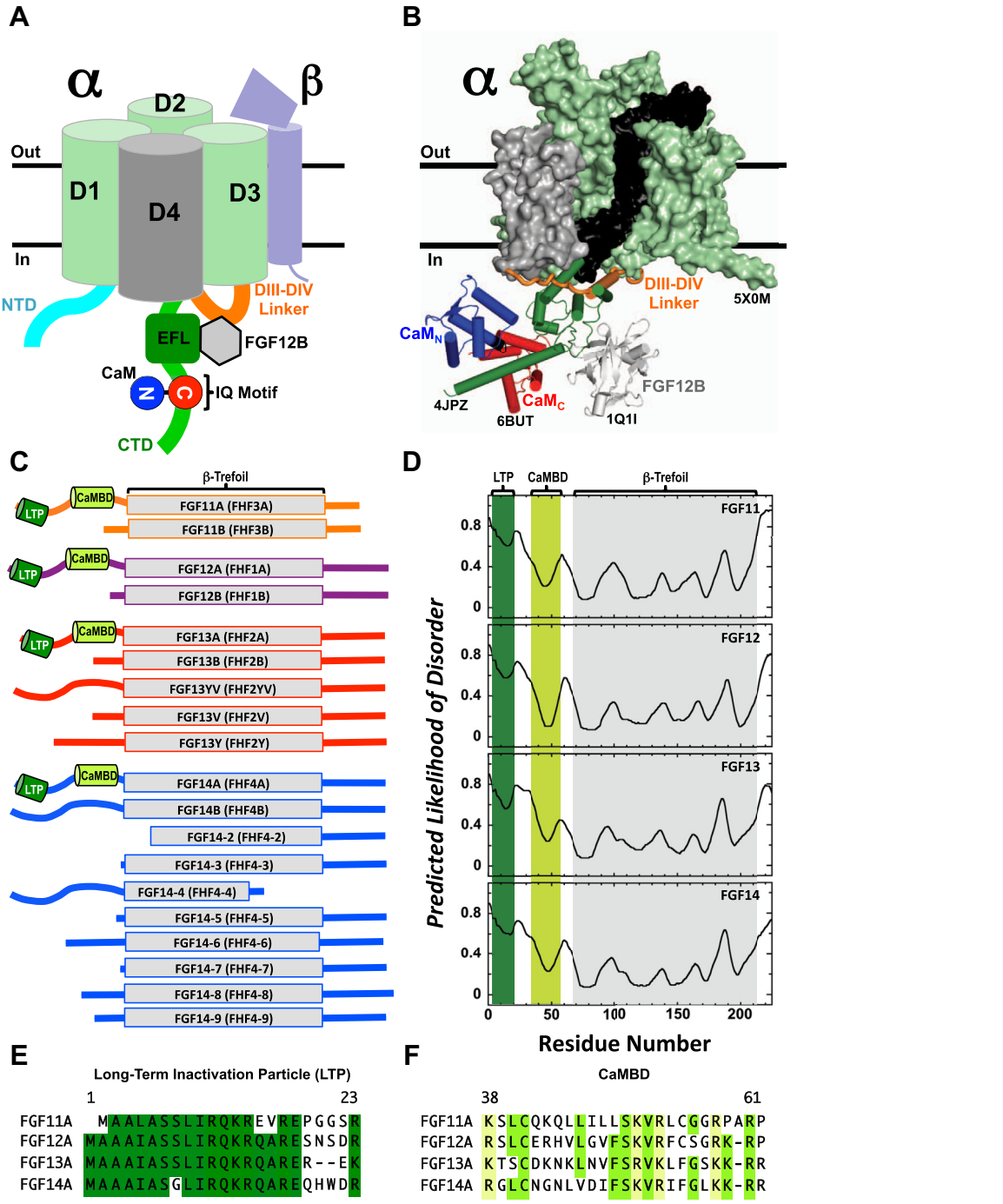

Figure 1. Architecture of Na_V, CaM, and FGFs. *A*, schematic of human Na_V. The α-subunit N-terminal domain (NTD, *cyan*), transmembrane domains DI-DIII (*pale green*) and DIV (*gray*), the linker connecting DIII to DIV (*orange*), and C-terminal domain (CTD, *green*) with 4-helix bundle EFL (*dark green*) that binds FGFs (*light gray*), and IQ motif that binds CaM (CaM_N/*blue*, CaM_C/*red*) are shown. Auxiliary β-subunit that contains a transmembrane helix and extracellular domain is *lavender*. *B*, model of apo CaM and FGF12B bound to Na_V. Model is comprised of Na_VPAS (5X0M, DI-DIII/*pale green surface*, DIV voltage-sensing domain/*gray surface*, DIV pore domain/*black surface*, DIII-DIV linker/*orange cartoon*), the $Na_V1.5_{CTD}$ (4DCK, *forest green*), the apo CaM+$Na_V1.2_{IQp}$ ensemble (6BUT, CaM_N/*blue*, CaM_C/*red*), and FGF12B (1Q1U, *gray*). The $Na_V1.5_{CTD}$ was aligned to Na_VPAS EFL (a.a. 1426–1521), the apo CaM+$Na_V1.2_{IQp}$ ensemble was aligned with 4DCK *via* CaM a.a. 101–112 and 117–128, and FGF12B was aligned with 4DCK using FGF13B a.a. 11–158. For simplicity $Na_V1.2_{IQp}$ in 6BUT and CaM FGF13B in 4DCK are not shown. *C*, schematics of FGF11 (*orange*), FGF12A (*purple*), FGF13A (*red*), and FGF14 (*blue*) splice variants. The β-trefoil core is shown as a *rectangle*, and the long-term inactivation particle (LTP, *green*) and putative CaM-binding domain (CaMBD, *limon*) are shown as cylinders. *D*, predicted likelihood of disorder of A-type FGF isoform sequences. The minima shaded *green* and *limon* correspond to the LTP and CaMBD sequences, respectively. The folded β-trefoil core is shaded *gray*. *E* and *F*, sequence alignments of the A-type FGF LTP (*E*) and CaMBD (*F*). Positions that are conserved in at least three of the four FGF isoforms are shaded (LTP/*green*, CaMBD/*limon*). Positions in the CaMBD (*F*) that contain a basic K or R in all four isoforms are shaded in *pale yellow*. Alignments were made with COBALT (108).

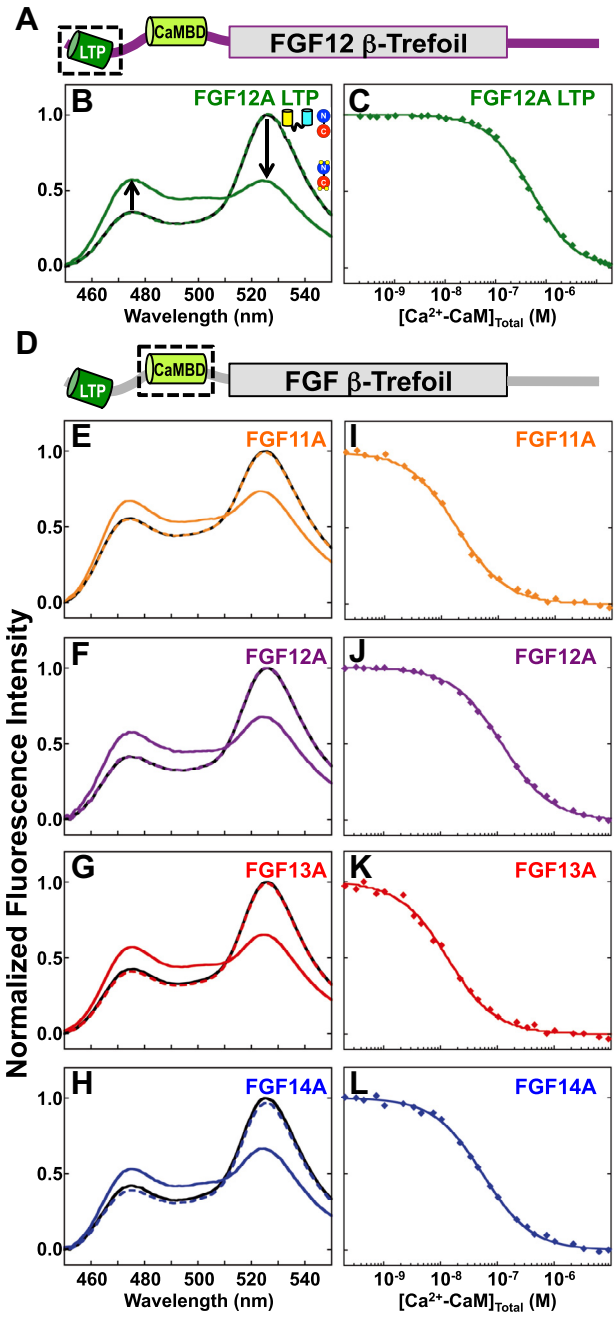

Figure 2. $(Ca^{2+})_4$-CaM binds the $FGF12A_{LTP}$ and FGF CaMBD biosensors. *A*, schematic of FGF12A. Folded β-trefoil core is shown as a *rectangle*, and LTP (*green*) and CaMBD (*limon*) are shown as *cylinders*. The *black box* indicates the position of the FGF12A LTP. *B*, steady-state emission spectra of the $FGF12A_{LTP}$ biosensor alone (*solid black*), in the presence of apo (*dashed green*) and $(Ca^{2+})_4$-CaM (*solid green*). *C*, equilibrium titration of $FGF12A_{LTP}$ biosensor with $(Ca^{2+})_4$-CaM (*green*). *D*, schematic of an A-type FGF. Folded β-trefoil core is shown as a *rectangle*, and LTP (*green*) and CaMBD (*limon green*) are shown as *cylinders*. The *black box* indicates the position of the A-type FGF CaMBD. *E–H*, steady-state fluorescence spectra of $FGF11A_{CaMBD}$ (*E*, *orange*), $FGF12A_{CaMBD}$ (*F*, *purple*), $FGF13A_{CaMBD}$ (*G*, *red*), $FGF14A_{CaMBD}$ (*H*, *blue*) biosensors alone (all shown in *solid black*), and in the presence of apo (*dashed/colored*) and $(Ca^{2+})_4$-CaM (*solid/colored*). *I–L*, equilibrium titrations of $FGF11A_{CaMBD}$ (*I*), $FGF12A_{CaMBD}$ (*J*), $FGF13A_{CaMBD}$ (*K*), and $FGF14A_{CaMBD}$ (*L*) biosensors with $(Ca^{2+})_4$-CaM. FGF isoforms are colored as in panels *E–H*.

sequence of the LTP of FGF12A ($FGF12A_{LTP}$, residues 1–23) or CaMBD of FGF11A ($FGF11A_{CaMBD}$, residues 36–62), FGF12A ($FGF12A_{CaMBD}$, residues 38–64), FGF13A ($FGF13A_{CaMBD}$, residues 35–60), and FGF14A ($FGF14A_{CaMBD}$, residues 37–63) was inserted between YFP and CFP (see Experimental procedures).

Table 1
FGF biosensor affinities for WT CaM

FGF_{LTP}	ΔG^a	K_d^b	N
$FGF12A_{LTP}$	−8.42 ± 0.24	576 nM	11
FGF_{CaMBD}	**ΔG^a**	**K_d^b**	
$FGF11A_{CaMBD}$	−10.43 ± 0.18	19 nM	7
$FGF12A_{CaMBD}$	−9.40 ± 0.21	107 nM	9
$FGF13A_{CaMBD}$	−10.63 ± 0.02	13 nM	6
$FGF14A_{CaMBD}$	−9.87 ± 0.18	51 nM	7

[a] ΔG in kcal/mol. Average and standard deviation based on N determinations of biosensors prepared from at least two independent cultures.
[b] K_d, equilibrium dissociation constant, calculated from average value of ΔG reported in this table. Solution Conditions: 50 mM HEPES, 100 mM KCl, 50 μM EGTA, 5 mM NTA, 1 mM $MgCl_2$, 1.5 μM BSA, 500 μM DTT, 1 mM $CaCl_2$; pH 7.4, 22 °C.

Addition of excess apo CaM to the $FGF12A_{LTP}$ biosensor (200:1 [CaM]:[Biosensor]) caused negligible (∼0%) changes in the emission spectrum (Fig. 2, *A* and *B*). However, after addition of saturating Ca^{2+}, reciprocal changes were observed in the intensities of YFP (reduced by ∼50%) and CFP (increased by ∼52%) (Fig. 2*B*). This indicated that $(Ca^{2+})_4$-CaM, but not apo CaM, bound to $FGF12A_{LTP}$. Equilibrium titrations of the $FGF12A_{LTP}$ biosensor with $(Ca^{2+})_4$-CaM showed that the K_d was 576 nM (Fig. 2*C*, Table 1).

As observed for $FGF12A_{LTP}$, addition of excess apo CaM to the $FGF11A_{CaMBD}$, $FGF12A_{CaMBD}$, $FGF13A_{CaMBD}$, or $FGF14A_{CaMBD}$ biosensor (200:1 [CaM]:[Biosensor]) resulted in negligible spectral changes, while $(Ca^{2+})_4$-CaM induced robust reciprocal changes in the intensities of YFP (-21%–33%) and CFP (18%–32%) (Fig. 2, *D–H*). Equilibrium titrations with $(Ca^{2+})_4$-CaM showed that CaM bound the CaMBD of each FGF isoform with a different affinity (Fig. 2, *I–L*, Table 1), with FGF13A being most favorable (K_d = 13 nM) and FGF12A least favorable (K_d = 107 nM). The small difference in the affinity of $(Ca^{2+})_4$-CaM for the CaMBD of FGF11A and FGF13A (0.18 kcal/mol) was statistically significant (*p* value 0.02358) but would have a very small effect on saturation.

These affinities were 5–44-fold more favorable than the affinity of $(Ca^{2+})_4$-CaM for the FGF12A LTP (Fig. 2, *C* and *I–L*, Table 1). Based on the high degree of conservation in the LTP sequence of all four FGFs, these findings suggest that when a single $(Ca^{2+})_4$-CaM is bound to a full-length A-type FGF, it would occupy the putative CaMBD rather than the LTP.

Both CaM_N and CaM_C are required for tight binding to FGF CaMBDs

We assessed the energetic contributions of CaM_N and CaM_C to the binding of $FGF12A_{CaMBD}$ and $FGF13A_{CaMBD}$. Initial titrations with isolated CaM_N (aa 1–80) or CaM_C (aa 76–148) showed no evidence of binding at a concentration of 1 μM (data not shown). Because the interaction of CaM with $FGF12A_{CaMBD}$ and $FGF13A_{CaMBD}$ is Ca^{2+}-dependent, the energetic contributions of CaM_N and CaM_C within full-length CaM were explored by determining their affinity for "knockout mutants" of CaM engineered to significantly reduce Ca^{2+}-binding to one domain. In these mutants the bidentate

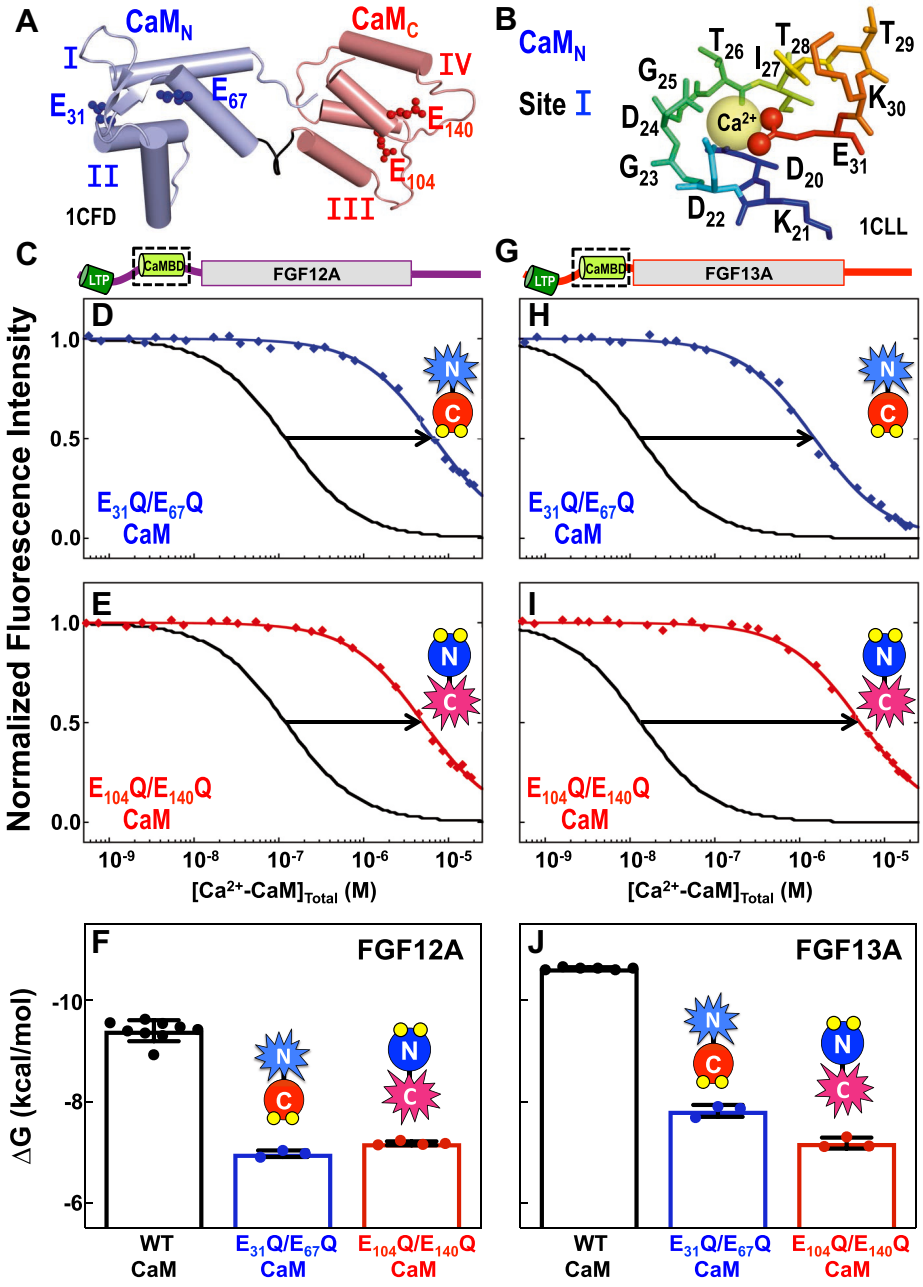

Figure 3. Energetic contribution of CaM_N and CaM_C to FGF12A and FGF13A CaMBD binding by CaM. *A*, position of E31 (*blue*), E67 (*blue*), E104 (*red*), and E140 (*red*), shown as ball-and-stick, in apo CaM (1CFD, CaM_N/*light blue*, CaM_C/*salmon*). *B*, $(Ca^{2+})_4$-CaM site I (1CLL): Ca^{2+} (*yellow sphere*) is surrounded by residues D20 (*blue*) to E31 (*red*). The coordinating O atoms of E31 are shown as *red spheres*. *C*, schematic of FGF12A. Folded β-trefoil core is shown as a *rectangle*, and LTP (*green*) and CaMBD (*limon*) are shown as *cylinders*. The *black box* indicates the position of the FGF12A CaMBD. *D* and *E*, equilibrium titrations of the $FGF12A_{CaMBD}$ biosensor with E31Q/E67Q (*D*, *blue*) or E104A/E140Q CaM (*E*, *red*). A reference titration with WT CaM is shown in *black*. *F*, ΔG of WT (*black*), E31Q/E67Q (*blue*), and E104Q/E140Q (*red*) CaM binding the $FGF12A_{CaMBD}$ biosensor. *G*, schematic of FGF13A. Folded β-trefoil core is shown as a *rectangle*, and LTP (*green*) and CaMBD (*limon*) are shown as *cylinders*. The *black box* indicates the position of the FGF13A CaMBD. *H* and *I*, equilibrium titrations of the $FGF13A_{CaMBD}$ biosensor with E31Q/E67Q (*H*, *blue*) or E104A/E140Q CaM (*I*, *red*). A reference titration with WT CaM is shown in *black*. *J*, ΔG of WT (*black*), E31Q/E67Q (*blue*), and E104Q/E140Q (*red*) CaM binding the $FGF13A_{CaMBD}$ biosensor.

Glu (position 12) in sites I and II (E31Q/E67Q) or sites III and IV (E104Q/E140Q) was replaced with Gln (Fig. 3, *A* and *B*) (31). In these mutants with one domain mutated, the other domain retains a high Ca^{2+}-binding affinity (31).

Equilibrium titrations of $FGF12A_{CaMBD}$ with these mutants showed that E31Q/E67Q CaM bound to the CaMBD with a K_d of 6.74 μM, a 63-fold lower affinity than WT CaM, while E104Q/E140Q CaM bound with a K_d of 4.73 μM, a 44-fold lower affinity (Fig. 3, *C–E*, Table 2). The affinities of the knockout mutants were very close (Fig. 3*F*), suggesting that CaM_N and CaM_C contribute similarly to binding $FGF12A_{CaMBD}$. Compared with the pattern observed for $FGF12A_{CaMBD}$, the threefold difference in the affinity of E31Q/E67Q CaM (K_d = 1.59 μM, 122-fold weaker than WT) and E104Q/E140Q CaM (K_d = 4.73 μM, 363-fold weaker than WT) (Fig. 3, *G–I*, Table 2) for $FGF13A_{CaMBD}$ indicated that CaM_C

Table 2
FGF biosensor affinities for mutant CaM

	$FGF12A_{CaMBD}$			$FGF13A_{CaMBD}$		
CaM_{1-148}	ΔG[a]	K_d[b]	N	ΔG[a]	K_d[b]	N
E31Q/E67Q	−6.98 ± 0.07	6.74 μM	3	−7.82 ± 0.12	1.59 μM	3
E104Q/E140Q	−7.18 ± 0.04	4.73 μM	4	−7.18 ± 0.11	4.72 μM	3

[a] ΔG in kcal/mol. Average and standard deviation based on N titrations of biosensors prepared from at least two independent cultures.
[b] K_d, equilibrium dissociation constant, calculated from average value of ΔG reported in this table. Solution Conditions: 50 mM HEPES, 100 mM KCl, 50 μM EGTA, 5 mM NTA, 1 mM $MgCl_2$, 1.5 μM BSA, 500 μM DTT, 1 mM $CaCl_2$; pH 7.4, 22 °C.

makes an energetic contribution to binding $FGF13A_{CaMBD}$ that is larger than that made by CaM_N.

The mutant E104Q/E140Q CaM contains only a functional CaM_N. Given that its affinity for $FGF13A_{CaMBD}$ and $FGF12A_{CaMBD}$ was identical (Fig. 3, *F* and *J*, Table 2), this suggests that the separation in the affinity of WT CaM for the CaMBD of FGF12A and FGF13A may result from differences in the interface between CaM_C and the CaMBD.

Stoichiometry of copurified $(Ca^{2+})_4$-CaM+FGF NTD complexes

The finding that $(Ca^{2+})_4$-CaM can bind to the isolated FGF LTP (Fig. 2, *A–C*) and CaMBD (Fig. 2, *D–L*) suggests that the NTD of an A-type FGF may bind two molecules of CaM simultaneously. To test this hypothesis, we utilized revered-phase high-performance liquid chromatography (rpHPLC) to determine the molar ratio of $(Ca^{2+})_4$-CaM to FGF NTD in copurified complexes of $(Ca^{2+})_4$-CaM bound to NTD fragments (residues ∼1–70, containing both the LTP and CaMBD), of FGF11A ($FGF11A_{NTD}$), FGF12A ($FGF12A_{NTD}$), FGF13A ($FGF13A_{NTD}$), and FGF14A ($FGF14A_{NTD}$) (Fig. S4, *A* and *B*).

In rpHPLC chromatograms (Fig. S4*B*) of the copurified complexes, the ratio of the integrated area under the absorbance peaks corresponding to the FGF NTD and $(Ca^{2+})_4$-CaM showed that each sample contained a 1:1 M ratio of $(Ca^{2+})_4$-CaM to FGF NTD (Fig. S4*C*). This is consistent with the isolated NTD fragment of each A-type FGF binding a single molecule of $(Ca^{2+})_4$-CaM following copurification. However, these results do not indicate the location(s) of CaM and do not discriminate among the possibilities of having a single $(Ca^{2+})_4$-CaM bound to an LTP or CaMBD site alone, or possibly bridging these two sites with one CaM domain bound to each. Furthermore, these results do not preclude the possibility that a second molecule of $(Ca^{2+})_4$-CaM may bind the NTD if the local CaM concentration was sufficiently high.

CaM_N and CaM_C bind identically to $FGF12A_{CaMBDp}$ and $FGF12A_{NTD}$

Solution NMR is uniquely capable of monitoring changes in the local environment of individual residues within a protein. To determine how the two domains of $(Ca^{2+})_4$-CaM rearrange and interact with an FGF NTD at a one-to-one molar ratio, solution NMR was used to monitor FGF12A CaMBD and $FGF12A_{NTD}$-induced changes in the local environment of residues in labeled $(Ca^{2+})_4$-CaM.

We first sought to determine how binding of the isolated CaMBD of FGF12A (Fig. 4*A*) changed CaM_N and CaM_C within $(Ca^{2+})_4$-CaM. To do this we compared the ^{15}N-HSQC spectrum of ^{15}N-$(Ca^{2+})_4$-CaM bound to an unlabeled C-terminal fragment of the $FGF12A_{NTD}$ (^{14}N-$FGF12A_{CaMBDp}$, residues 41–70), corresponding to roughly half of the $FGF12A_{NTD}$, to spectra of isolated $(Ca^{2+})_2$-CaM_N (Fig. 4*B*) and $(Ca^{2+})_2$-CaM_C (Fig. 4*C*). These showed that $FGF12A_{CaMBDp}$ binding induced changes in the chemical shifts of residues throughout CaM_N and CaM_C, which is consistent with both domains of $(Ca^{2+})_4$-CaM interacting directly with $FGF12A_{CaMBDp}$.

To determine how $(Ca^{2+})_4$-CaM interacts with the full NTD that contains both the LTP and CaMBD sequences (Fig. 4*D*), we compared the ^{15}N-HSQC spectrum of ^{15}N-$(Ca^{2+})_4$-CaM bound to the complete unlabeled NTD of FGF12A (^{14}N-$FGF12A_{NTD}$) to that of ^{15}N-$(Ca^{2+})_4$-CaM bound to the ^{14}N-$FGF12A_{CaMBDp}$. As observed in the 1:1 complex of CaM bound to the $FGF12A_{CaMBDp}$, the binding of $FGF12A_{NTD}$ changed the local environment of residues throughout CaM_N (Fig. S5, *A* and *B*) and CaM_C (Fig. S5, *C* and *D*). This conclusion alone would be consistent with either CaM bridging the LTP and CaMBD or CaM binding either of these sites exclusively.

Comparison of the ^{15}N-HSQC spectrum of ^{15}N-$(Ca^{2+})_4$-CaM+^{14}N-$FGF12A_{CaMBDp}$ to that of ^{15}N-$(Ca^{2+})_4$-CaM+^{14}N-$FGF12A_{NTD}$ revealed that peaks corresponding to $(Ca^{2+})_4$-CaM residues were in nearly identical positions in both spectra (Fig. 4*E*). This indicated that residues in $(Ca^{2+})_4$-CaM have equivalent local environments when bound to the $FGF12A_{CaMBDp}$ or $FGF12A_{NTD}$, suggesting that the interface between $(Ca^{2+})_4$-CaM and the $FGF12A_{NTD}$ is identical to that of $(Ca^{2+})_4$-CaM+$FGF12A_{CaMBDp}$ (Fig. 4*F*). The simplest explanation is that $(Ca^{2+})_4$-CaM binds the $FGF12A_{NTD}$ exclusively through the CaMBD, with neither domain of CaM making persistent contacts with the LTP. There was no evidence for more than one conformation though we cannot exclude the possibility that some additional conformations were populated in low abundance.

$FGF12A_{CaMBDp}$ and $FGF12A_{NTD}$ respond similarly to $(Ca^{2+})_4$-CaM binding

To probe the interface between $(Ca^{2+})_4$-CaM and the $FGF12A_{NTD}$ from the FGF side, we used solution NMR to examine the effect of unlabeled $(Ca^{2+})_4$-CaM (^{14}N-$(Ca^{2+})_4$-CaM) binding on the local chemical environment of residues in the labeled $FGF12A_{CaMBDp}$ (^{15}N-$FGF12A_{CaMBDp}$) and

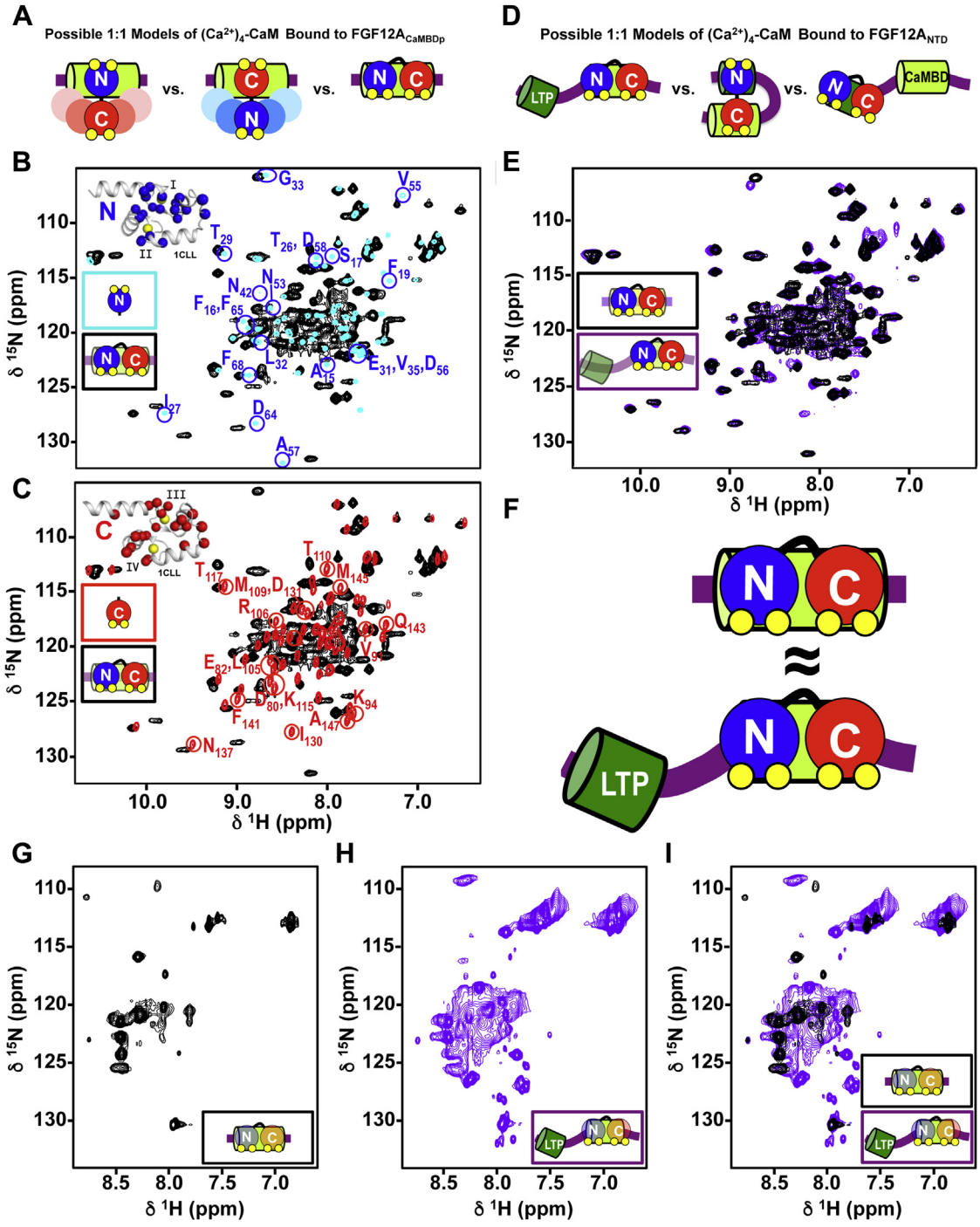

Figure 4. Interaction of $(Ca^{2+})_4$-CaM with the $FGF12A_{CaMBDp}$ and $FGF12A_{NTD}$. *A*, schematics depicting models of $(Ca^{2+})_4$-CaM (CaM_N/*blue*, CaM_C/*red*) binding to the $FGF12A_{CaMBDp}$ (*limon cylinder*) in a 1: 1 M ratio. *B* and *C*, overlay of the ^{15}N-HSQC spectra of ^{15}N-$(Ca^{2+})_2$-CaM_N (*blue*, *B*) or ^{15}N-$(Ca^{2+})_2$-CaM_C (*red*, *C*) and ^{15}N-$(Ca^{2+})_4$-CaM+^{14}N-$FGF12A_{CaMBDp}$ (*black*). Peaks labeled in the spectrum of ^{15}N-$(Ca^{2+})_2$-CaM_N (*B*) or ^{15}N-$(Ca^{2+})_2$-CaM_C (*C*) are shifted in the ^{15}N-$(Ca^{2+})_4$-CaM+^{14}N-$FGF12A_{CaMBD}$ spectrum. *Insets* show the Cα of labeled CaM_N (*blue spheres*, *B*) or CaM_C (*red spheres*, *C*) residues on a structure of $(Ca^{2+})_4$-CaM (1CLL, *gray helices*). *D*, schematics depicting models of $(Ca^{2+})_4$-CaM (CaM_N/*blue*, CaM_C/*red*) binding to the $FGF12A_{NTD}$ in a 1:1 M ratio. FGF12A LTP (*green*) and CaMBD (*limon*) are shown as cylinders. *E*, overlay of the ^{15}N-HSQC spectra of ^{15}N-$(Ca^{2+})_4$-CaM bound to the ^{14}N-$FGF12A_{CaMBDp}$ (*black*) or ^{14}N-$FGF12A_{NTD}$ (*purple*). *F*, schematic showing that the interface is essentially identical between $(Ca^{2+})_4$-CaM (CaM_N/*blue*, CaM_C/*red*) and the $FGF12A_{CaMBDp}$ (*limon cylinder*) or $FGF12A_{NTD}$ (LTP/*green cylinder*, CaMBD/*limon cylinder*). *G* and *H*, ^{15}N-HSQC spectrum of ^{14}N-$(Ca^{2+})_4$-CaM bound to ^{15}N-$FGF12A_{CaMBDp}$ (G, *black*) or ^{15}N-$FGF12A_{NTD}$ (*H*, *purple*). *I*, overlay of the ^{15}N-HSQC spectra of ^{14}N-$(Ca^{2+})_4$-CaM bound to ^{15}N-$FGF12A_{CaMBDp}$ (*black*) or ^{15}N-$FGF12A_{NTD}$ (*purple*).

$FGF12A_{NTD}$ (^{15}N-$FGF12A_{NTD}$). The isolated $FGF12A_{CaMBDp}$ and $FGF12A_{NTD}$ were not soluble at the concentrations needed for NMR studies. Thus, we made a pairwise comparison of the local chemical environment of FGF residues in ^{15}N-$FGF12A_{CaMBDp}$ (Fig. 4*G*) to those in ^{15}N-$FGF12A_{NTD}$ (Fig. 4*H*) when each was bound to ^{14}N-$(Ca^{2+})_4$-CaM. This was illuminating regarding the preference of CaM for the CaMBD sequence relative to the LTP sequence.

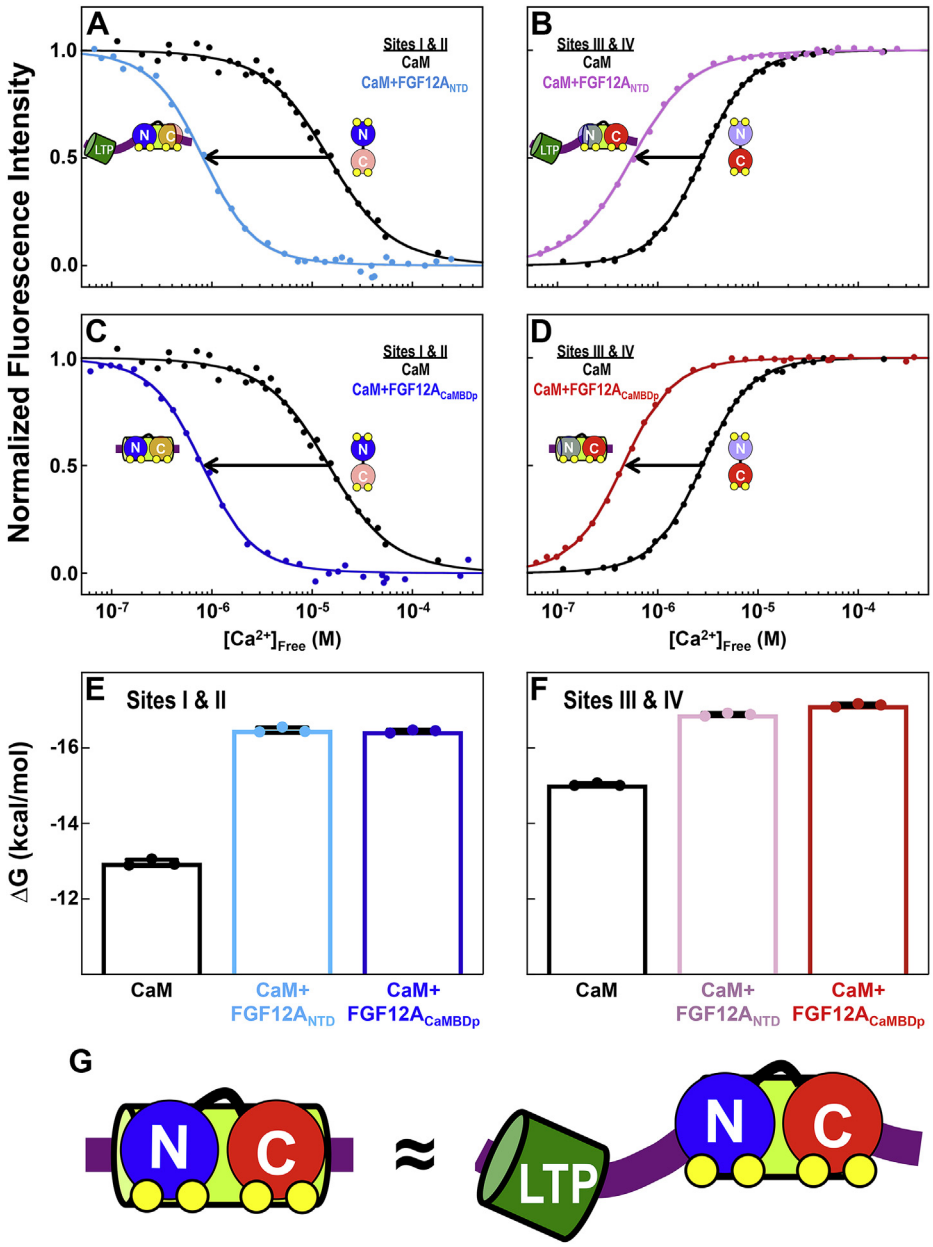

Figure 5. Equilibrium Ca^{2+} titrations of CaM+FGF12A$_{CaMBDp}$ and CaM+FGF12A$_{NTD}$. *A*, equilibrium Ca^{2+} titrations of sites I and II of CaM alone (*black*) and in the presence of the FGF12A$_{NTD}$ (*teal*). *B*, equilibrium Ca^{2+} titrations of sites III and IV of CaM alone (*black*) and in the presence of the FGF12A$_{NTD}$ (*pink*). *C*, equilibrium Ca^{2+} titrations of sites I and II of CaM alone (*black*) and in the presence of the FGF12A$_{CaMBDp}$ (*blue*). *D*, equilibrium Ca^{2+} titrations of sites III and IV of CaM alone (*black*) and in the presence of the FGF12A$_{CaMBDp}$ (*red*). *E* and *F*, ΔG of Ca^{2+} binding to sites I and II (*E*) in CaM alone (*black*), +FGF12A$_{NTD}$ (*teal*) or +FGF12A$_{CaMBDp}$ (*blue*), and sites III and IV (*F*) in CaM alone (*black*), +FGF12A$_{NTD}$ (*pink*) or +FGF12A$_{CaMBDp}$ (*red*). *G*, schematic depicting that the interface is essentially identical between $(Ca^{2+})_4$-CaM (CaM$_N$/*blue*, CaM$_C$/*red*) and the FGF12A$_{CaMBDp}$ (*lime green cylinder*) or FGF12A$_{NTD}$ (LTP/*green cylinder*, CaMBD/*limon cylinder*).

The majority of the peaks in the ^{15}N-HSQC spectrum of ^{15}N-FGF12A$_{CaMBDp}$ or ^{15}N-FGF12A$_{NTD}$ bound to ^{14}N-$(Ca^{2+})_4$-CaM had a ^{1}H chemical shift between 8.0 and 8.5 ppm (Fig. 4, *G* and *H*). Peaks in the^{15}N-HSQC spectrum of ^{14}N-$(Ca^{2+})_4$-CaM+^{15}N-FGF12A$_{CaMBDp}$ were relatively well dispersed (Fig. 4*G*), which was likely due to the small size of this peptide (30 FGF12A residues with a four-residue tag). In contrast, the spectrum of ^{14}N-$(Ca^{2+})_4$-CaM+^{15}N-FGF12A$_{NTD}$ was more crowded, as expected for a larger fragment (70 FGF12A residues with a four-residue tag) (Fig. 4*H*). The higher degree of overlap in that spectrum likely reflects the presence of a disordered linker between the LTP and CaMBD, as predicted in the Robetta models of full-length FGF12A (Fig. S3, *B–H*).

To assess whether the pattern of peaks in the ^{15}N-HSQC spectra of ^{14}N-$(Ca^{2+})_4$-CaM+^{15}N-FGF12A$_{CaMBDp}$ and ^{14}N-$(Ca^{2+})_4$-CaM+^{15}N-FGF12A$_{NTD}$ were consistent with the predicted α-helical secondary structure of the FGF12A LTP and CaMBD, the observed peak positions were compared with those predicted with SPARTA+ (55) for residues 41–70

Table 3
Effect of $FGF12A_{CaMBDp}$ and $FGF12A_{NTD}$ on Ca^{2+} binding of CaM

	Sites I and II			Sites III and IV		
CaM_{1-148}	ΔG_1[a] (kcal/mol)	ΔG_2[a] (kcal/mol)	$K_{d\text{-}app}$[b] (μM)	ΔG_1[a] (kcal/mol)	ΔG_2[a] (kcal/mol)	$K_{d\text{-}app}$[b] (μM)
-	−6.27 ± 0.21	−12.96 ± 0.09	15.92	−6.77 ± 0.09	−15.03 ± 0.04	2.73
+ $FGF12A_{CaMBDp}$	−7.75 ± 0.07	−16.45 ± 0.04	0.81	−8.08 ± 0.14	−17.14 ± 0.05	0.45
+ $FGF12A_{NTD}$	−7.69 ± 0.04	−16.48 ± 0.07	0.79	−8.27 ± 0.08	−16.89 ± 0.04	0.56

Solution conditions: 50 mM HEPES, 100 mM KCl, 1 mM $MgCl_2$, 50 μM EGTA, 5 mM NTA, 1 mM DTT, pH 7.4, 22 °C.
[a] Average ΔG values based on three independent determinations. Titrations fit to Equation 4.
[b] $K_{d\text{-}app}$ (apparent dissociation constant) was calculated from half of the average ΔG_2 value reported in this table.

($FGF12A_{CaMBDp}$) and 1–70 ($FGF12A_{NTD}$) (Fig. S6, *A–D*) from the model of full-length FGF12A. Peak positions in the ^{15}N-HSQC spectra of ^{14}N-$(Ca^{2+})_4$-CaM+^{15}N-$FGF12A_{CaMBDp}$ (Fig. S6*C*) or +^{15}N-$FGF12A_{NTD}$ (Fig. S6*D*) agreed well with those predicted from the fragments of the FGF12A model. We inferred that both the FGF12A LTP and CaMBD adopted an α-helical structure in the complexes of $(Ca^{2+})_4$-CaM bound to the $FGF12A_{CaMBDp}$ or $FGF12A_{NTD}$.

Comparison of the ^{15}N-HSQC spectrum of ^{14}N-$(Ca^{2+})_4$-CaM+^{15}N-$FGF12A_{CaMBDp}$ (Fig. 4*G*) to that of ^{14}N-$(Ca^{2+})_4$-CaM+^{15}N-$FGF12A_{NTD}$ (Fig. 4*H*) showed that a subset of peaks in the ^{14}N-$(Ca^{2+})_4$-CaM+^{15}N-$FGF12A_{NTD}$ spectrum were located at positions essentially equivalent to those of peaks in the ^{14}N-$(Ca^{2+})_4$-CaM+^{15}N-$FGF12A_{CaMBDp}$ spectrum (Fig. 4*I*). This suggests that these peaks correspond to the same residues in the $FGF12A_{CaMBDp}$ and $FGF12A_{NTD}$ and that they have an essentially identical local chemical environment when bound by $(Ca^{2+})_4$-CaM. That supports a model where $(Ca^{2+})_4$-CaM is anchored to the $FGF12A_{NTD}$ *via* the CaMBD sequence when in a one-to-one complex as shown schematically in Figure 4*F*.

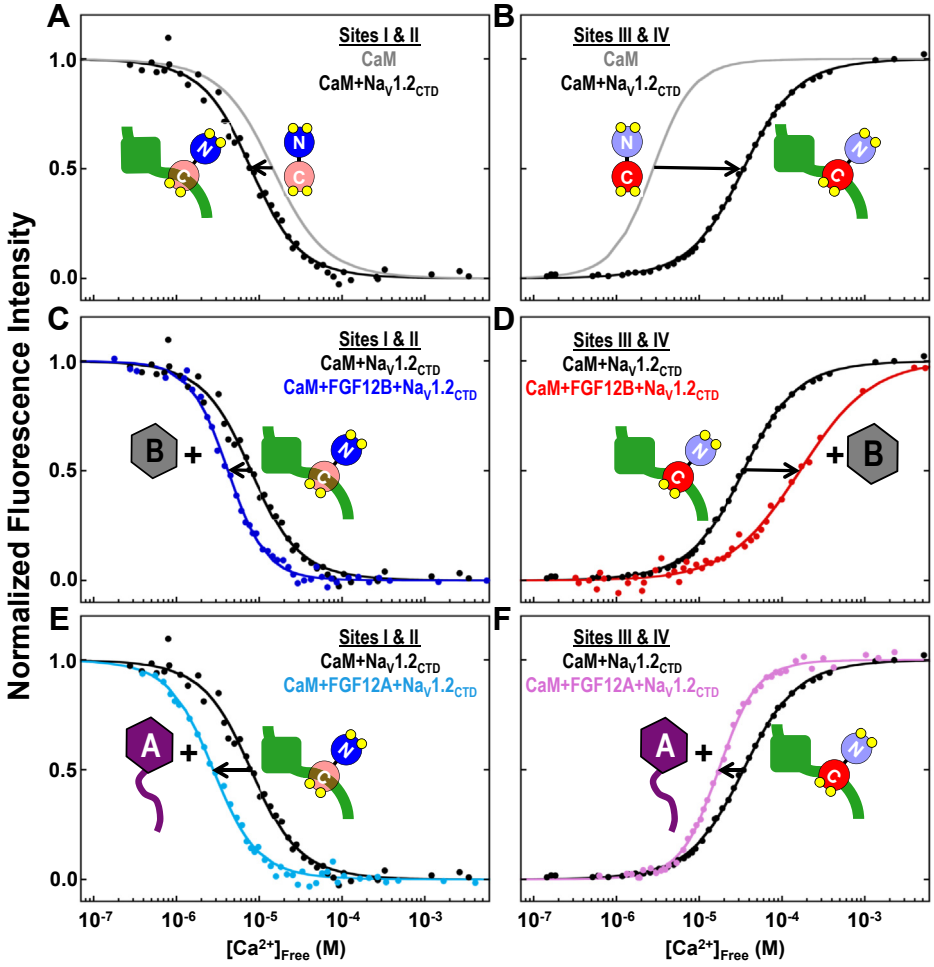

Figure 6. Equilibrium Ca^{2+} titrations of CaM+FGF12B+$Na_V1.2_{CTD}$ and CaM+FGF12A+$Na_V1.2_{CTD}$. *A* and *B*, equilibrium Ca^{2+} titrations of sites I and II (*A*), and sites III and IV (*B*) of CaM in CaM+$Na_V1.2_{CTD}$. Solid gray lines show reference Ca^{2+} titrations sites I and II (*A*) and sites III and IV (*B*) of CaM alone. *C*, *E*, equilibrium Ca^{2+} titrations of sites I and II of CaM in CaM+$Na_V1.2_{CTD}$ (*C*, *E*, *black*), CaM+FGF12B+$Na_V1.2_{CTD}$ (*C*, *blue*) and CaM+FGF12A+$Na_V1.2_{CTD}$ (*E*, *teal*). *D*, *F*, equilibrium Ca^{2+} titrations of sites III and IV of CaM in CaM+$Na_V1.2_{CTD}$ (*D*, *F*, *black*), CaM+FGF12B+$Na_V1.2_{CTD}$ (*D*, *red*) and CaM+FGF12A+$Na_V1.2_{CTD}$ (*F*, *pink*).

Table 4
Effect of FGFB and FGF12A on Ca^{2+} binding by CaM bound to $Na_V1.2_{CTD}$

CaM_{1-148}+ $Na_V1.2_{CTD}$	Ratio[a]	Sites I and II			Sites III and IV		
		ΔG_1[b] (kcal/mol)	ΔG_2[b] (kcal/mol)	$K_{d\text{-}app}$[c] (μM)	ΔG_1[b] (kcal/mol)	ΔG_2[b] (kcal/mol)	$K_{d\text{-}app}$[c] (μM)
–	–	−6.27 ± 0.39	−13.78 ± 0.08	7.91	−6.04 ± 0.19	−12.09 ± 0.07	33.42
+ FGF12B	1:1:1	−6.00 ± 0.10	−14.51 ± 0.09	4.51	−5.44 ± 0.11	−10.27 ± 0.11	157.67
+ FGF12A	1:1:1	−7.18 ± 0.22	−14.99 ± 0.08	2.82	−5.31 ± 0.07	−12.91 ± 0.10	16.61
CaM_{1-148}+ $Na_V1.2_{CTD}$	Ratio[a]	$\Delta G_{1\text{-}app}$[b] (kcal/mol)	$\Delta G_{2\text{-}app}$[b] (kcal/mol)	$K_{d\text{-}app}$[c] (μM)	$\Delta G_{1\text{-}app}$[d] (kcal/mol)	$\Delta G_{2\text{-}app}$[d] (kcal/mol)	$K_{d\text{-}app}$[c] (μM)
+ FGF12A	2:1:1	−7.59 ± 0.14	−15.41 ± 0.14	1.97	−7.61 ± 0.24	−16.05 ± 0.04	1.14
+ FGF12A	2:1:1	–	–	–	−5.03 ± 0.16	−10.89 ± 0.13	92.94

Solution Conditions: 50 mM HEPES, 100 mM KCl, 1 mM $MgCl_2$, 50 μM EGTA, 5 mM NTA, 1 mM DTT, pH 7.4, 22 °C. Fluorescence controls shown in Figures S7 and S8.
[a] Stoichiometry of CaM:$Na_V1.2_{CTD}$:FGF12B or CaM:$Na_V1.2_{CTD}$:FGF12B.
[b] Titrations fit to Equation 4. Average ΔG values based on three independent determinations monitoring Phe intensity.
[c] $K_{d\text{-}app}$ (apparent dissociation constant) was calculated from half of the average ΔG_2 value reported in this table.
[d] Titrations fit to Equation 5. Average ΔG based on three independent determinations monitoring Tyr intensity.

$FGF12A_{CaMBDp}$ and $FGF12A_{NTD}$ increase the Ca^{2+} affinity of CaM_N and CaM_C

To quantitatively assess the allosteric effect of $FGF12A_{NTD}$ and $FGF12A_{CaMBDp}$ on the Ca^{2+}-binding affinity of CaM_N and CaM_C, we conducted equilibrium Ca^{2+} titrations of CaM in the presence of the $FGF12A_{NTD}$ or $FGF12A_{CaMBDp}$ by monitoring changes in the steady-state fluorescence intensity of endogenous Phe and Tyr residues to detect Ca^{2+} binding by CaM_N and CaM_C, respectively (31).

Equilibrium Ca^{2+} titrations of CaM bound to $FGF12A_{NTD}$ showed it increased the Ca^{2+}-binding affinity of sites I and II in CaM_N ($K_{d\text{-}app}$ = 0.81 μM) by ∼20-fold (Fig. 5*A*, Table 3) and sites III and IV in CaM_C ($K_{d\text{-}app}$ = 0.45 μM) by approximately fivefold (Fig. 5*B*, Table 3) relative to free CaM. In a similar pattern, $FGF12A_{CaMBDp}$ increased the affinity of sites I and II ($K_{d\text{-}app}$ = 0.79 μM) by ∼20-fold relative to CaM alone (Fig. 5*C*, Table 3), while sites III and IV ($K_{d\text{-}app}$ = 0.56 μM) (Fig. 5*D*, Table 3) bound Ca^{2+} with an approximately fivefold higher affinity. Thus, $FGF12A_{NTD}$ and $FGF12A_{CaMBDp}$ increased the Ca^{2+}-binding affinity of CaM_N (Fig. 5*E*, no statistically significant difference between the effect of NTD and CaMBD) and CaM_C (Fig. 5*F*, with CaMBD having a larger effect by 0.25 kcal/mol). This is consistent with both domains of $(Ca^{2+})_4$-CaM binding $FGF12A_{NTD}$ exclusively through the CaMBD region and having an identical interface with both (Fig. 5*G*). This supports the interpretation of NMR data presented in Figure 4, *A*–*I* and the conclusion that the LTP does not participate in the CaM-FGF12A NTD interaction in a 1:1 complex.

FGF12B and FGF12A differ in effects on Ca^{2+} binding by CaM+$Na_V1.2_{CTD}$

In isolation, both $FGF12A_{NTD}$ and $FGF12A_{CaMBDp}$ increased the Ca^{2+}-binding affinity of CaM_N and CaM_C (Fig. 5, *A*–*D*). This suggests that the allosteric regulatory roles of FGF12A, which includes the NTD and FGF12B, will not differ because only the A-type splice variant will be capable of binding CaM. Currently there is no evidence of CaM binding to FGF12B.

To understand the complementary roles of CaM and FGF bound to Na_V channels, it would be ideal to determine the Ca^{2+} affinity of CaM in a ternary complex with FGF12A bound to a full-length $Na_V1.2$ channel in a plasma membrane and compare that with the Ca^{2+} affinity of CaM in a complex with FGF12B bound to an identical full-length $Na_V1.2$. However, no currently available method is capable of measuring this property in these large transmembrane complexes. Therefore, we investigated Ca^{2+} binding to CaM in soluble ternary complexes containing either full-length FGF12A or FGF12B bound to the $Na_V1.2_{CTD}$ that contains both the EFL domain and IQ motif.

Unlike the FGF12A NTD fragments, which had a low abundance of naturally occurring fluorophores (2 Phe, 0 Tyr, 0 Trp), FGF12B (8 Phe, 10 Tyr, 1 Trp), FGF12A (10 Phe, 10 Tyr, 1, Trp), and $Na_V1.2_{CTD}$ (9 Phe, 4 Tyr, 1 Trp) all contain multiple aromatic residues (Fig. S7*A*) that could quench or overwhelm signals coming from CaM. There is also a controversial report that the EFL of $Na_V1.5$ binds Ca^{2+} (56), and that phenomenon could contribute a Ca^{2+}-dependent change in fluorescence intensity coincident with that of the changes in CaM.

To determine whether the intrinsic fluorescence of FGF12B and $Na_V1.2_{CTD}$ was Ca^{2+}-dependent, titrations of the FGF12B+$Na_V1.2_{CTD}$ complex were conducted. Its signal was essentially flat (Ca^{2+}-independent) (Fig. S7, *B* and *C*), and its excitation (Fig. S7, *D* and *E*) and emission (Fig. S7, *F* and *G*) spectra were essentially identical under Ca^{2+}-depleted conditions and in excess Ca^{2+} ($[Ca^{2+}]_{Total}$ = 10 mM). Similarly, Ca^{2+} titrations of the FGF12A+$Na_V1.2_{CTD}$ complex (Fig. S8*A*) showed that its fluorescence intensity was essentially flat (Fig. S8, *B* and *C*), consistent with a lack of intrinsic Ca^{2+} binding by these FGF-Na_V complexes. Thus, in the Ca^{2+} titrations of CaM bound to FGF12B+$Na_V1.2_{CTD}$ or FGF12A+-$Na_V1.2_{CTD}$, the change in fluorescence intensity was interpreted as reporting solely on Ca^{2+} binding to CaM.

To understand the effect of full-length FGF12B or FGF12A on Ca^{2+} binding by CaM bound to the $Na_V1.2_{CTD}$, we compared the equilibrium Ca^{2+} titrations of the ternary complexes to those of the binary CaM+$Na_V1.2_{CTD}$ complex (Fig. 6, *A* and *B*). In CaM+$Na_V1.2_{CTD}$ the Ca^{2+} affinity of CaM sites I and II ($K_{d\text{-}app}$ = 7.91 μM, Fig. 6*A*, Table 4) increased approximately twofold compared with free CaM. This change

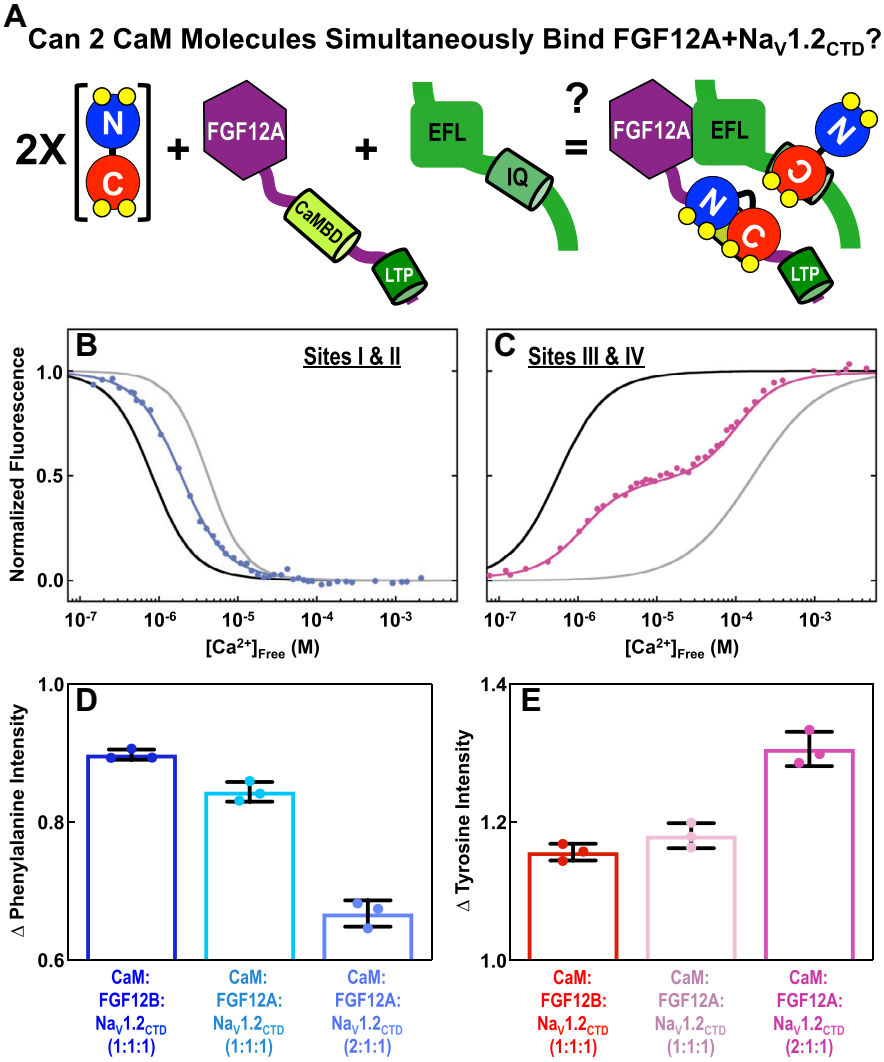

Figure 7. Equilibrium Ca^{2+} titrations of a 2:1:1 complex of CaM+FGF12A+Na$_V$1.2$_{CTD}$. *A*, schematic depicting the possible binding of two CaM (CaM_N/*blue*, CaM_C/*red*) molecules the FGF12A (*purple*)+Na$_V$1.2$_{CTD}$ (*green*) complex. The FGF12A LTP (*green*) and CaMBD (*limon*) are shown as *cylinders*. *B*, equilibrium Ca^{2+} titrations of CaM sites I and II in CaM+FGF12A+Na$_V$1.2$_{CTD}$ (*light blue*, CaM:FGF12A:Na$_V$1.2$_{CTD}$ = 2:1:1). The *solid black* and *gray lines* show reference titrations of CaM sites I and II in CaM+FGF12A$_{NTD}$ and CaM+FGF12B+Na$_V$1.2$_{CTD}$, respectively. *C*, Equilibrium Ca^{2+} titrations of sites III and IV of CaM in CaM+FGF12A+Na$_V$1.2$_{CTD}$ (*hot pink*, CaM:FGF12A:Na$_V$1.2$_{CTD}$ = 2:1:1). The *solid black* and *gray lines* show reference titrations of CaM sites III and IV in CaM+FGF12A$_{NTD}$ and CaM+FGF12B+Na$_V$1.2$_{CTD}$, respectively. *D*, maximum decrease in Phe fluorescence intensity in equilibrium Ca^{2+} titrations of CaM+FGF12B+Na$_V$1.2$_{CTD}$ (*blue*), CaM+FGF12A+Na$_V$1.2$_{CTD}$ (*teal*, CaM:FGF12A:Na$_V$1.2 = 1:1:1) and CaM+FGF12A+Na$_V$1.2$_{CTD}$ (*light blue*, CaM:FGF12A:-Na$_V$1.2$_{CTD}$ = 2:1:1). *E*, maximum increase in Tyr fluorescence intensity in equilibrium Ca^{2+} titrations of CaM+FGF12B+Na$_V$1.2$_{CTD}$ (*red*), CaM+FGF12A+-Na$_V$1.2$_{CTD}$ (*pink*, CaM:FGF12A:Na$_V$1.2 = 1:1:1), and CaM+FGF12A+Na$_V$1.2$_{CTD}$ (*hot pink*, CaM:FGF12A:Na$_V$1.2$_{CTD}$ = 2:1:1).

was nearly identical to the difference observed between sites I and II in a CaM_N fragment (residues 1–75) and in full-length CaM and was shown to reflect the release of anticooperative interactions between CaM_N and residues in the linker between CaM domains (30, 57). This indicates that Na$_V$1.2$_{CTD}$ binding perturbs the thermodynamic linkage between CaM_N and CaM_C.

In the CaM+Na$_V$1.2$_{CTD}$ complex, the Ca^{2+} affinity of sites III and IV decreased by ~12-fold ($K_{d\text{-}app}$ = 33.42 μM, Fig. 6*B*, Table 4) relative to free CaM, consistent with preferential binding of the Na$_V$1.2 IQ motif by apo versus $(Ca^{2+})_4$-CaM (22–25). Comparing the two domains of CaM to each other in the CaM+Na$_V$1.2$_{CTD}$ complex, CaM_N binds Ca^{2+} with a approximately fourfold higher affinity than CaM_C, indicating that Na$_V$1.2$_{CTD}$ binding reverses the sequential occupancy of the CaM domains observed in CaM alone (gray curves in Fig. 6, *A* and *B*).

In the ternary CaM+FGF12B+Na$_V$1.2$_{CTD}$ complex, a slight additional increase (approximately twofold) was observed in the Ca^{2+} affinity of sites I and II ($K_{d\text{-}app}$ = 4.51 μM) relative to CaM bound to the Na$_V$1.2$_{CTD}$ (Fig. 6*C*, Table 4). Inclusion of FGF12B decreased the Ca^{2+}-binding affinity of sites III and IV ($K_{d\text{-}app}$ = 157.67 μM) by approximately fivefold relative to CaM in the CaM+Na$_V$1.2$_{CTD}$ complex (Fig. 6*D*, Table 4). Thus, FGF12B binding to the Na$_V$1.2$_{CTD}$ further separated the midpoints of the Ca^{2+}-binding isotherms of CaM_N and CaM_C. This was an unanticipated result because there are no published reports of direct interactions between CaM and this

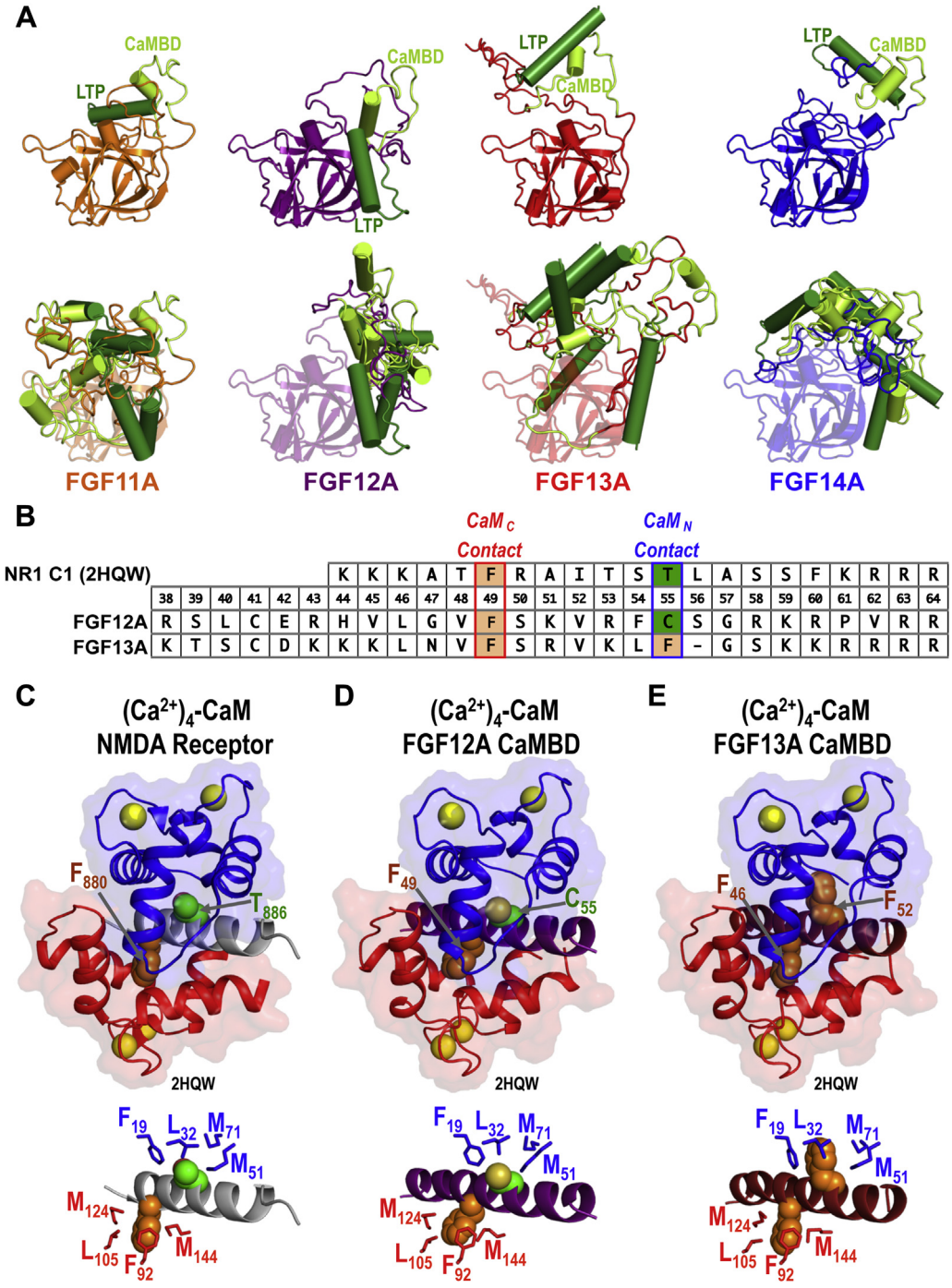

Figure 8. Models of $(Ca^{2+})_4$-CaM bound to the FGF12A and FGF13A CaMBD. In all structures CaM residues 1–75 are *blue*, 76–80 are *black* and 81–148/*red*, and Ca^{2+} are *yellow spheres*. *A*, *top*, model 1 in the Robetta (54) generated ensemble of each full-length A-type FGF. *Bottom*, orientation of the LTP and CaMBD regions in the modeled ensemble of FGF11, FGF12A, FGF13A, and FGF14. The FGF isoforms are colored as follows: FGF11A is *orange*, FGF12A is *purple*, FGF13A is *red*, and FGF14A is *blue*. The LTP and CaMBD regions of each FGF are shown in *green* and *limon*, respectively. Models were aligned with FGF12A a.a. 71–204. *B*, alignment of the NMDA receptor CaMBD, FGF12A CaMBD, and FGF13A CaMBD sequences. The positions that correspond to F880 and T886in the NMDA receptor are *shaded* (hydrophobic/*tan*, polar/*green*). C: Structure of $(Ca^{2+})_4$-CaM bound to the NMDA receptor CaMBD (2HQW, *gray*), F880 (*orange*), and T886 (*green*) of the NMDA receptor are shown as *spheres* (*top*) and positions of F19, L32, M51, and M71 in CaM_N (*blue*) and F92, L105, M124, and M144 in CaM_C (*red*) are shown as *sticks* relative to F880 (*orange spheres*) and T886 (*green spheres*) in the NMDA receptor CaMBD (*lower*). D: Model of $(Ca^{2+})_4$-CaM bound to the FGF12A CaMBD (*purple*), F49 (*orange*), and C55 (*green*) of FGF12A are shown as spheres (*top*) and positions of F19, L32, M51, and M71 in CaM_N (*blue*) and F92, L105, M124, and M144 in CaM_C (*red*) are shown as sticks relative to F49 (*orange spheres*) and C55 (*green spheres*) in the FGF12A CaMBD (*bottom*). *E*, model of $(Ca^{2+})_4$-CaM bound to the FGF13A CaMBD (firebrick), F46 and F52 of FGF13A are shown as orange spheres (*top*) and positions of F19, L32, M51, and M71 in CaM_N (*blue*) and F92, L105, M124, and M144 in CaM_C (*red*) are shown as sticks relative to F46 (*orange spheres*) and C52 (*green spheres*) in the FGF13A CaMBD (*bottom*).

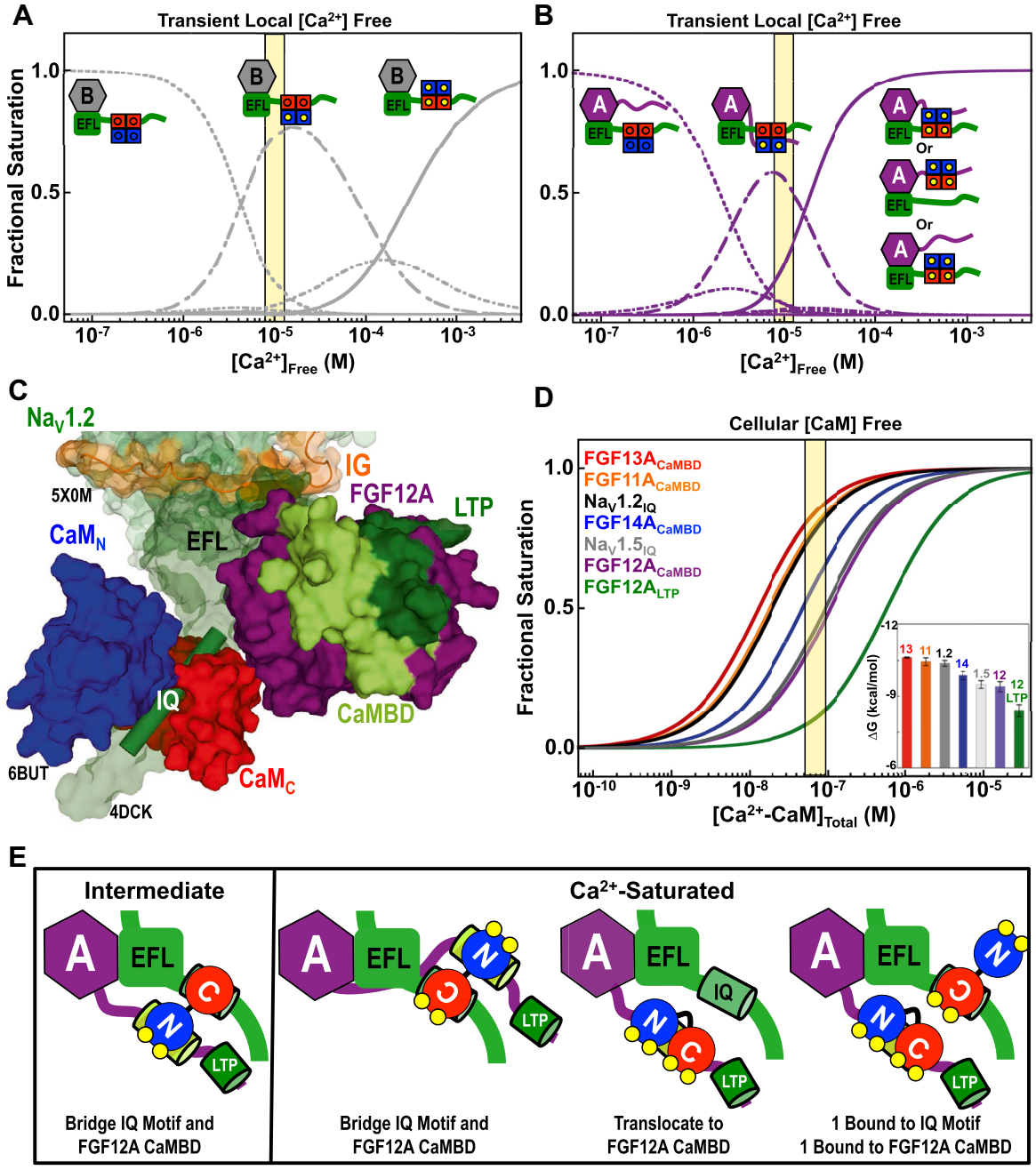

Figure 9. States of CaM bound to FGF12B+$Na_V1.2_{CTD}$ or FGF12A+$Na_V1.2_{CTD}$. *A* and *B*, abundance of ligated CaM species in the CaM+FGF12B+$Na_V1.2_{CTD}$ (*A*, *gray*) and CaM+FGF12A+$Na_V1.2_{CTD}$ (*B*, *purple*) complexes. Simulations are based on the Ca^{2+}-binding affinities reported in Table 4. States of CaM with an abundance >0.25 are shown in the inset schematics that depict the possible orientations of the CaM domains (CaM_N/*blue*, CaM_C/*red*) relative to FGF12B (*gray*) and $Na_V1.2_{CTD}$ (*green*) (*A*) or FGF12A (purple) and $Na_V1.2_{CTD}$ (*green*) (*B*), Ca^{2+} are shown as *yellow circles*. The *yellow box* is centered at physiologically relevant Ca^{2+} concentration of 10 μM. Representing the occupancy of the four Ca^{2+}-binding sites in CaM (in order I, II, III, IV) with binary, where 0 is emtpy and 1 if filled, the discernible (abundances >0.05) species of CaM in the CaM+FGF12B+$Na_V1.2_{CTD}$ complex (*A*) are 0000 (*dotted line*), 1100 (*dashed* and *dotted line*), 1101 or 1110 (*dashed line*), and 1111 (*solid line*). The discernible (abundance >0.5) species of CaM in the CaM+FGF12A+$Na_V1.2_{CTD}$ complex (*B*) are 0000 (*dotted line*), 1000 or 0100 (*dashed line*), 1100 (*dashed* and *dotted line*), 1111 (*solid line*). *C*, model of CaM (CaM_N/*blue*, CaM_C/*red*) bound to an Na_V CTD (*forest green*, surface) relative to the Na_V DIII-DIV linker (*orange*) and FGF12A (*purple*, LTP/*green*, CaMBD/*limon*). The model is a composite of $Na_V1.5$ CTD (4DCK), aligned with Na_VPAS (5X0M) EFL (a.a. 1426–1521). Na_VPAS a.a. 1122–1160 are shown as the DIII–DIV linker. The apo CaM+$Na_V1.2_{IQp}$ ensemble (6BUT) was aligned with 4DCK via CaM a.a. 101–112 and 117–128. The $Na_V1.2_{IQp}$ (a.a. 1904–1924) is shown as a *forest green cylinder*. The model of FGF12A was aligned with 4DCK using FGF13U a.a. 11–158. For clarity CaM and FGF13B in 4DCK are hidden. *D*, simulation of the saturation of each A-type FGF CaMBD (FGF11A/*orange*, FGF12A/*purple*, FGF13A/*red*, FGF14A/*blue*), FGF12A LTP (*green*) or the IQ motifs of $Na_V1.2$ (*black*) and $Na_V1.5$ (*gray*) with $(Ca^{2+})_4$-CaM. Simulations of $(Ca^{2+})_4$-CaM binding the FGF12A LTP and each FGF CaMBD are based on the affinities reported in Table 1. Simulations of $(Ca^{2+})_4$-CaM binding to IQ motifs are based on K_d of 19.8 nM for $Na_V1.2$ and 92.3 nM for $Na_V1.5$ (data not shown). The yellow shaded region highlights the estimated concentration range of free CaM (90) within the cell. The *inset* shows the ΔG of $(Ca^{2+})_4$-CaM binding to the putative A-type FGF CaMBDs (FGF11A/*orange*, FGF12A/*purple*, FGF13A/*red*, and FGF14/*blue*), FGF12A LPTD (*green*) and the $Na_V1.2$ IQ motif (*black*) and $Na_V1.5$ IQ motif (*gray*). The affinities are arranged from tightest (*left*) to weakest (*right*). *E*, schematic depiction of different models of partially ($(Ca^{2+})_2$-CaM_N, apo CaM_C) and fully Ca^{2+}-saturated CaM (CaM_N/*blue*, CaM_C/*red*) binding to the IQ motif (*green cylinder*) in $Na_V1.2_{CTD}$ (*green*) and/or FGF12A CaMBD (*limon cylinder*) in full-length FGF12A (*purple*). The FGF12A LTP is shown as a *green cylinder* and Ca^{2+} is shown as *yellow circles*.

shorter FGF12 splice variant that consists primarily of the folded β-trefoil core (Fig. 1*C*).

For CaM in CaM+FGF12A+$Na_V1.2_{CTD}$, the Ca^{2+} affinity of sites I and II ($K_{d\text{-}app}$ = 2.82 μM) was more favorable than those sites in CaM+$Na_V1.2_{CTD}$ (approximately threefold) or CaM+FGF12B+$Na_V1.2_{CTD}$ (approximately twofold) (Fig. 6, *C* and *E*, Table 4). The binding of FGF12A also increased the Ca^{2+} affinity of sites III and IV ($K_{d\text{-}app}$ = 16.61 μM) relative to CaM in both the CaM+$Na_V1.2_{CTD}$ (approximately twofold) and CaM+FGF12B+$Na_V1.2_{CTD}$ (approximately tenfold) complexes. The increased Ca^{2+}-binding affinity of both CaM domains in the CaM+FGF12A+$Na_V1.2_{CTD}$ complex is consistent with $(Ca^{2+})_4$-CaM interacting favorably with the NTD of full-length FGF12A when bound to the $Na_V1.2_{CTD}$.

Binding of multiple CaM molecules to the FGF12A+$Na_V1.2_{CTD}$ complex

Ca^{2+}-saturated CaM can bind two sites in the FGF12A NTD (Fig. 2, *A–L*) and one site in the $Na_V1.2$ IQ motif (22–25). Thus, at high local concentrations of Ca^{2+} and CaM, the CTD of $Na_V1.2$ channels with FGF12A bound might bind up to three molecules of $(Ca^{2+})_4$-CaM. However, $(Ca^{2+})_4$-CaM binds more weakly to the LTP than the CaMBD (Fig. 2, *C* and *J*, Table 1), and the solution NMR data were consistent with $(Ca^{2+})_4$-CaM binding the $FGF12A_{NTD}$ exclusively through the CaMBD region in a one-to-one complex (Fig. 4, *E* and *I*).

To explore the limits of stoichiometry, we tested whether FGF12A+$Na_V1.2_{CTD}$ might recruit a total of two molecules of CaM: one at the $Na_V1.2$ IQ motif and one at the FGF12A CaMBD (Fig. 7*A*). To do this, Ca^{2+} titrations were conducted of the CaM+FGF12A+$Na_V1.2_{CTD}$ complex at a [CaM]:[FGF12A]:[$Na_V1.2_{CTD}$] ratio of 2:1:1 (CaM+FGF12A+$Na_V1.2_{CTD}$ (2:1:1)). In this complex it was anticipated that CaM_N would not interact with the IQ motif regardless of the Ca^{2+} concentration (25) and that it would bind the FGF CaMBD only under Ca^{2+}-saturating conditions. In contrast, CaM_C would bind to the $Na_V1.2$ IQ motif constitutively (±Ca^{2+}), but CaM_C of a second -$(Ca^{2+})_4$-CaM molecule might bind at the FGF CaMBD.

The Ca^{2+} titrations of CaM_N in CaM+FGF12A+$Na_V1.2_{CTD}$ (2:1:1) were monotonic (Fig. 7*B*, *light blue line*). Sites I and II bound Ca^{2+} with an affinity ($K_{d\text{-}app}$ = 1.97 μM) that was between that of CaM in the CaM+$FGF12A_{NTD}$ ($K_{d\text{-}app}$ = 0.81 μM, Fig. 7*B*, *black line*) and CaM+FGF12B+$Na_V1.2_{CTD}$ ($K_{d\text{-}app}$ = 4.51 μM, Fig. 7*B*, *gray line*, Table 4) complexes.

The Ca^{2+} titrations of CaM_C in the CaM+FGF12A+$Na_V1.2_{CTD}$ (2:1:1) were biphasic (Fig. 7*C*, *red line*), in contrast to the titrations of CaM+FGF_{NTD} (Fig. 5*B*) and CaM+FGF12A+$Na_V1.2_{CTD}$ with a 1:1:1 stoichiometry (Fig. 6*F*). Fitting these data as a sum of two isotherms (see Experimental procedures), we determined that the dissociation constant of the first phase ($K_{d\text{-}app}$ = 1.14 μM) was similar to that of CaM_C in CaM+$FGF12A_{NTD}$ ($K_{d\text{-}app}$ = 0.45 μM, Fig. 7*C*, *black line*) while the dissociation constant of the second phase was similar to that of CaM_C in CaM+FGF12B+$Na_V1.2_{CTD}$ ($K_{d\text{-}app}$ = 157.67 μM, Fig. 7*C*, *gray line*, Table 4).

Both the shape of the Ca^{2+} titration curve of CaM sites III and IV in the 2:1:1 complex and the values of the resolved dissociation constants for each transition suggest that the FGF12A+$Na_V1.2_{CTD}$ complex can bind two CaM molecules simultaneously. Consistent with this, the change in intensity of both the Phe (Fig. 7*D*) and Tyr (Fig. 7*E*) signals observed in titrations of the CaM+FGF12A+$Na_V1.2_{CTD}$ (2:1:1) complex was approximately twofold larger than in Ca^{2+} titrations of CaM+FGF12B+$Na_V1.2_{CTD}$ or CaM+FGF12A+$Na_V1.2_{CTD}$.

The biphasic titration curves of the CaM_C sites and the changes in affinity of CaM_N and CaM_C in the CaM+FGF12A+$Na_V1.2_{CTD}$ (2:1:1) complex were consistent with FGF12A+$Na_V1.2_{CTD}$ binding two molecules of CaM simultaneously with one molecule of CaM bound *via* the FGF12A CaMBD and the other bound at the $Na_V1.2$ IQ motif. This suggests that if local concentrations of Ca^{2+} and CaM were sufficiently high, $Na_V1.2$ channels that have FGF12A associated may recruit a second molecule of CaM through the FGF12A CaMBD independent of CaM binding at the $Na_V1.2$ IQ motif.

Discussion

Under resting conditions, the cytosolic CTD of Na_V channels binds one FGF and one CaM (16, 17, 22, 48); however, the mechanism by which these two auxiliary proteins modulate channel function is poorly understood. The thermodynamic and structural studies presented here show a direct, Ca^{2+}-dependent interaction between $(Ca^{2+})_4$-CaM and the NTD of the four A-type FGF splice variants. We found that (a) $(Ca^{2+})_4$-CaM preferentially binds a CaMBD in the NTD with a dissociation constant in the low nM range but can bind the LTP with weaker affinity, and (b) both domains of $(Ca^{2+})_4$-CaM bind the CaMBD. These results suggest that at elevated cytosolic Ca^{2+} concentrations reached during an action potential, CaM may translocate from the Na_V IQ motif to the FGF CaMBD and participate in regulatory functions previously identified as requiring FGF binding to Na_Vs.

Discovery of novel $(Ca^{2+})_4$-CaM-binding sites

Members of the intracellular FGF subfamily were reported to directly bind Na_V isoforms (17, 18), voltage-gated potassium channels (58), and islet brain protein 2 (59). A recent report proposed an interaction between CaM and FGF12B when bound to $Na_V1.4$ (52); however, there has been no evidence for a direct interaction between CaM and any FGF isoform. Using multiple spectroscopic methods, we have demonstrated that the isolated LTP (Fig. 2, *B* and *C*) and CaMBD (Fig. 2, *E–L*) sequences of A-type FGFs bind $(Ca^{2+})_4$-CaM but not apo CaM(Fig. 2, *B* and *E–H*), mirroring the selectivity of CaMBD sequences in targets such as CaMKII (60), myosin light chain kinase (61), and calcineurin (62).

Robetta models of all four full-length A-type FGFs (Fig. 8*A*) predicted that segments of both LTP and CaMBD sequences would adopt α-helical structure. For FGF12A, this was supported by the ^{15}N-HSQC spectra of ^{15}N-$FGF12A_{CaMBDp}$ and

^{15}N-FGF12A$_{NTD}$ with one bound $(Ca^{2+})_4$-CaM (Fig. 4, *G–I*, Fig S6, *C* and *D*). The energetically similar models for each FGF show an ensemble of positions for the LTP and CaMBD separated by a disordered linker. The full NTD is tethered to the β-trefoil core with a disordered linker (Fig. 8*A*). In solution, this would allow the LTP and CaMBD to move independently relative to each other and the β-trefoil core. This flexibility and range of motion may facilitate $(Ca^{2+})_4$-CaM binding the FGF NTD when the β-trefoil core is bound to a Na_V EFL.

$(Ca^{2+})_4$-CaM is known to bridge noncontiguous sites as observed in structures of CaM bound to the STRA6 retinol receptor (63) and the SK channel (64)., However, comparison of NMR spectra (Fig. 4*E*) and effects of FGF12A$_{CaMBDp}$ and FGF12A$_{NTD}$ on Ca^{2+} binding by CaM (Fig. 5, *A–F*, Table 3) were consistent with $(Ca^{2+})_4$-CaM binding the FGF12A NTD exclusively at the CaMBD site. This suggests that $(Ca^{2+})_4$-CaM would bind the NTD of the other A-type FGF isoforms (11A, 13A, and 14A) exclusively through the CaMBD in a one-to-one complex. However, the ability of $(Ca^{2+})_4$-CaM to bind the isolated FGF12A LTP (and its nearly identical sequence in all four A-type FGFs) suggests that if the local CaM concentration is high, the LTP site could recruit a second molecule of CaM to an A-type FGF. Although $(Ca^{2+})_4$-CaM binds to CaMBD with higher affinity than to LTP, CaM might interact transiently with LTP before binding to CaMBD. The reported thermodynamic studies were conducted under equilibrium conditions and did not address kinetics or explore possible translocation between the sites.

Differences in $(Ca^{2+})_4$-CaM-FGF CaMBD interface

The two-domain architecture of CaM allows it to recognize target sequences in a variety of ways, with some targets such as Na_V and myosin IQ motifs (65), binding a single domain of CaM (CaM_C) while others, such as CaMKII (66), bind both. Titrations of the FGF12A and FGF13A CaMBD with E31Q/E67Q CaM (Fig. 3, *D* and *H*) and E104Q/E140Q CaM (Fig. 3, *E* and *I*), and the ^{15}N-HSQC spectra of labeled $(Ca^{2+})_4$-CaM bound to the unlabeled FGF12A$_{CaMBDp}$ (Fig. 4, *B* and *C*) or FGF12A$_{NTD}$ (Fig. 4*E*, and Fig. S5, *A–D*) were consistent with both CaM domains recognizing FGF CaMBD sequences. However, the approximately tenfold difference in the affinity between FGF13A and FGF12A indicates that their CaM–FGF interfaces differ.

To explore possible structural sources for this disparity, we modeled the $(Ca^{2+})_4$-CaM– FGF12A CaMBD interface on a high-resolution structure (2HQW.pdb) of $(Ca^{2+})_4$-CaM bound to the NR1C1 site of the N-methyl-D-aspartate (NMDA) receptor (67, 68). In 2HQW, F880 binds the hydrophobic cleft of CaM_C while T886 is the primary contact in the cleft of CaM_N (Fig. 8, *B* and *C*). An alignment of NR1C1 with the CaMBDs of FGF12A and FGF13A (Fig. 8*D*) suggested that CaM_C would bind a Phe in each FGF CaMBD (F49 in FGF12A or F46 in FGF13A) (Fig. 8, *B–E*). However, CaM_N would contact a Cys (C55) in FGF12A (Fig. 8*D*) and a Phe (F52) in FGF13A (Fig. 8*E*). In homology models of $(Ca^{2+})_4$-CaM bound to the FGF12A (Fig. 8*D*) and FGF13A CaMBD (Fig. 8*E*), based on 2HQW and minimized using YASARA, the hydrophobic pocket of CaM_N would make more favorable close contacts with the bulkier F52 in FGF13A than with the smaller polar C55 of FGF12A. This may explain the approximately tenfold higher affinity of $(Ca^{2+})_4$-CaM for FGF13A CaMBD.

The structural models shown in Figure 8, *D* and *E* were simulated assuming that CaM binds to both FGF12A and FGF13A in an antiparallel arrangement (*i.e.*, CaM_N binds the C-terminal half of the CaMBD) that is observed for the majority of CaM–target interactions. However, the binding of knockout mutants having only one functional domain suggests another possible arrangement. We found that Ca^{2+}-saturated E104Q/E140Q CaM (functionally equivalent to apo CaM_C tethered to $(Ca^{2+})_2$-CaM_N) bound the FGF12A and FGF13A CaMBDs with nearly identical affinity (Fig. 3, *E*, *F*, *I*, and *J*). A simple interpretation would be that those titrations represent binding of $(Ca^{2+})_2$-CaM_N to a similar half-site in each FGF CaMBD. Thus, the disparity in the affinity might arise from differences in the interface between CaM_C and FGF CaMBDs.

The ability of CaM_N and CaM_C to recognize a variety of target sequences (68) makes it extremely difficult to predict their orientation on a CaMBD. There are high-resolution structures of some peptides bound to $(Ca^{2+})_4$-CaM in a parallel orientation. The ability of the hydrophobic clefts of CaM_N and CaM_C to form more favorable interactions with a Phe versus Cys may cause the functional domain in each CaM knockout mutant to compete for the same sequence in the FGF12A CaMBD, as was previously observed in the binding of $(Ca^{2+})_4$-CaM to melittin (69). In that complex, the single Trp residue of melittin preferentially binds to CaM_C in full-length CaM, and CaM_N interacts elsewhere; however, CaM_N as an isolated fragment will bind to the Trp residue that is available because CaM_C is absent.

In the titrations of the FGF12A$_{CaMBD}$ biosensor with E104Q/E140Q CaM, the functional CaM_N may interact with F49 in the FGF12A CaMBD. This would make the interface between E104Q/E140Q CaM with the CaMBD of either FGF12A or FGF13A similar, which could explain the nearly identical affinity of E104Q/E140Q CaM for these sequences.

Although $(Ca^{2+})_4$-CaM was modeled according to the more common antiparallel orientation, CaM could recognize the FGF12A and FGF13A CaMBD in a parallel orientation as seen in structures of $(Ca^{2+})_4$-CaM bound to IQ motif peptides from $Ca_V1.2$, $Ca_V2.2$, and $Ca_V2.3$ (70, 71) and a CaMBD from CaM-dependent kinase kinase (72). Alternatively, $(Ca^{2+})_4$-CaM might bind the CaMBD of FGF12A in an orientation opposite from that adopted when binding to FGF13A. Crystal structures have shown a Ca_V target peptide bound to CaM in both parallel and antiparallel orientations (71, 73) and TFP, an antipsychotic drug that binds $(Ca^{2+})_4$-CaM, has also been found in opposing orientations (74–76).

In the future, high-resolution structures of $(Ca^{2+})_4$-CaM bound to the FGF12A and FGF13A CaMBD will be required to determine the positions of CaM_N and CaM_C and how differences in the interface between CaM and these FGF CaMBDs contribute to free energies of binding.

FGF12B lowers Ca^{2+} affinity of CaM_C bound to $Na_V1.2_{CTD}$

In high-resolution structures of apo CaM bound to $Na_V1.5$ CTD fragments in the presence or absence of a B-type FGF, the interface between apo CaM_C and the Na_V IQ motif is essentially identical (28, 51). Although two residues (Y98 and K144) in the β-trefoil core of the B-type splice variant of FGF13 (FGF13U) are within 5 Å of residues K95 and N111 in CaM_C in a crystallographic structure of apo CaM bound to the $Na_V1.5$ CTD with FGF13U (51), no interface is observed between CaM_C and FGF13U in this structure. The simplest conclusion is that the interaction of CaM_C at the Na_V IQ motif is independent of B-type FGF binding to Na_V EFL. However, binding of FGF12B to CaM+$Na_V1.2_{CTD}$ decreased the Ca^{2+} affinity of sites III and IV in CaM_C (Fig. 6*D*, Table 4). Thermodynamic linkage requires that FGF12B allosterically alters the energy of CaM binding to $Na_V1.2_{CTD}$.

Because CaM is a highly acidic protein (pI ∼ 4) and FGF12B is basic (pI ∼ 9), we hypothesized that FGF12B may increase the affinity of apo CaM for the $Na_V1.2_{CTD}$ through favorable electrostatic interactions. However, in superpositions of apo and (Ca^{2+})$_4$-CaM bound to the $Na_V1.2_{CTD}$ with either FGF12B or FGF12A (Fig. 9*C* and Fig. S9, *A*–*D*), the nearest residues in apo CaM_C (K94) or (Ca^{2+})$_2$-CaM_C (I130 and R126) and the large basic patch in the β-trefoil core of FGF12B (K117) or FGF12A (K193) are separated by > 13 Å. Thus, it is unlikely that electrostatic interactions between CaM_C and FGF12B are sufficient to explain the FGF12B-induced changes in the energetics of CaM association with the $Na_V1.2_{CTD}$.

Ca^{2+} binding to CaM_C induces a ∼180° rotation of CaM_C on the $Na_V1.2$ IQ motif (25). This may require transient release and reassociation of CaM_C with the $Na_V1.2$ IQ motif, which in turn might be facilitated by conformational flexibility (*i.e.*, a hinge) between the EFL and IQ motif of $Na_V1.2$. In crystallographic structures containing an Na_V CTD bound by FGF12B or FGF13U, the FGF contacts both the Na_V EFL and residues that precede the IQ motif (26, 51). This suggests that the binding of FGF12B may alter the dynamics between the $Na_V1.2$ EFL and IQ motif, which could perturb the ability of CaM_C to reassociate with the $Na_V1.2$ IQ motif following a Ca^{2+}-induced release.

Ca^{2+} ligation states of CaM bound to $Na_V1.2$

Based on the Ca^{2+} affinities of the CaM domains when bound to FGF12B+$Na_V1.2_{CTD}$ or FGF12A+$Na_V1.2_{CTD}$, we predict that, at high cytosolic Ca^{2+} concentrations (∼10 μM (77)), $Na_V1.2$ associated with FGF12B will have either apo CaM or half-saturated ((Ca^{2+})$_2$-CaM_N, apo CaM_C) CaM bound (Fig. 9*A*). In contrast, channels bound to FGF12A are expected to be populated by apo, half ((Ca^{2+})$_2$-CaM_N, apo CaM_C), and fully Ca^{2+}-saturated CaM (Fig. 9*B*). Thus, $Na_V1.2$ with either FGF12 splice variant bound could undergo regulatory processes requiring only apo CaM or Ca^{2+} binding solely to the sites in CaM_N. However, only $Na_V1.2$ bound to FGF12A would support modulation requiring Ca^{2+}-induced rotation or release of CaM from the $Na_V1.2$ IQ motif.

The effect of FGF binding on Na_V function has been shown to depend upon the FGF splice variant bound (21, 43, 46, 47). Multiple splice variants of a particular FGF isoform have been found to be expressed simultaneously (38, 78), suggesting that within a cell, Na_Vs would be associated with more than one. Their unique effects on Na_V function have been proposed to correlate with variations in their NTD sequences. While it is unclear how CaM and the FGFs modulate Na_V function, the FGF splice variant-dependent differences in the available states of CaM during a spike in the local Ca^{2+} concentration could contribute to their unique effects on the functional states of Na_V.

Cellular competition for (Ca^{2+})$_4$-CaM

Both CaM and FGF colocalize with Na_V (19, 47, 50, 79, 80). Because both apo and (Ca^{2+})$_4$-CaM bind Na_V IQ motifs with high affinity (22–28) and the β-trefoil cores of FGF12 and FGF13 also bind Na_V CTD fragments with high affinity (20, 40), it is likely that CaM and an FGF are constitutively associated with an Na_V (Fig. 9*C*). Proteomic studies investigating $Na_V1.2$-associated proteins in rat neurons have found a level of CaM and FGF enrichment in pull-downs of the $Na_V1.2$ α-subunit similar to other constitutively associated proteins such as the Na_V β-subunit β2 (16).

Our thermodynamic and structural studies suggest that at elevated cytosolic Ca^{2+} levels, an FGF CaMBD and Na_V IQ motif will compete for (Ca^{2+})$_4$-CaM in an isoform-dependent manner (Fig. 9*D*) due to their proximity and similar affinities for (Ca^{2+})$_4$-CaM. The FGF12A-induced increase in the Ca^{2+} affinity of both CaM domains when bound to the $Na_V1.2_{CTD}$ (Fig. 6, *E* and *F*) suggests that CaM translocates from the Na_V IQ motif to the FGF CaMBD at elevated cytosolic Ca^{2+} concentrations.

Table 5
FGF biosensor sequences

FGF_{LTP}	Start Position[a]	Sequence[b]	End Position[a]	pI[c]
$FGF12A_{LTP}$	1	MAAAIASSLIRQKRQARESNSDR	23	11.54
FGF_{CaMBD}	**Start Position[a]**	**Sequence[b]**	**End Position[a]**	**pI[c]**
$FGF11A_{CaMBD}$	36	KSLCQKQLLILLSKVRLCGGRPARPDR	62	10.95
$FGF12A_{CaMBD}$	38	RSLCERHVLGVFSKVRFCSGRKRPVRR	64	11.88
$FGF13A_{CaMBD}$	35	KTSCDKNKLNVFSRVKLFGSKKRRRR	60	11.85
$FGF14A_{CaMBD}$	37	KTSCDKNKLNVFSRVKLFGSKKRRRR	63	11.85

[a] Start and end positions are numbered according to the UniProt (https://www.uniprot.org/) convention (106).
[b] FGF sequence inserted between the sequences for the YFP and CFP fluorophores in the FGF biosensor constructs (at KpnI and AgeI restriction sites).
[c] Theoretical isoelectric point calculated with ExPASy (https://web.expasy.org/protparam/) (107).

While the nine Na_V and four FGF isoforms have tissue-dependent patterns of expression, multiple isoforms of both are expressed in some tissues (38, 42, 45, 81, 82), implying that multiple Na_V-FGF pairings are present across tissues as well as within a particular cell. The different possible forms of FGF CaMBD and Na_V IQ motif recognition by $(Ca^{2+})_4$-CaM may have distinct effects on channel function and could provide a means to elicit unique modulation of Na_V by Ca^{2+}, CaM, and FGF in different tissues and potentially across channels within a particular cell. Structural and functional studies investigating $(Ca^{2+})_4$-CaM bound to complexes composed of CTD fragments of other Na_V isoforms and FGF11A, FGF13A or FGF14A will be needed to determine the generality of the allosteric effects of FGFs on Ca^{2+} binding by CaM observed in this study

Stoichiometry of CaM bound to Na_V

The Ca^{2+} titrations of CaM+FGF12A+$Na_V1.2_{CTD}$ (2:1:1) were consistent with the FGF12A+$Na_V1.2_{CTD}$ complex binding one molecule of CaM at the FGF12A CaMBD and one at the $Na_V1.2$ IQ motif (Fig. 7, *B–D*, Table 4). This may allow Na_V channels to recruit a second molecule of CaM, as has been reported for $Ca_V1.2$ (50, 83). The ability of the FGF CaMBD to anchor a CaM molecule to an Na_V may explain the results of a recent report that found FGF13A is sufficient to regulate arrhythmogenic late current in cardiac $Na_V1.5$ channels with an IQ>AA mutation that blocks CaM binding (44). Although those channels would not have CaM bound at the IQ motif, our findings predict that the NTD of FGF13A would bind $(Ca^{2+})_4$-CaM, which might be sufficient for regulation if the primary role of the IQ motif is to serve as a sink of constitutively bound CaM.

The closely related channel $Na_V1.4$, primarily found in skeletal muscle, bound only a single molecule of CaM in HEK293 cells under resting conditions and during spikes in cytosolic Ca^{2+} (50). That 1:1 stoichiometry may be related to the fact that HEK293 cells do not express any A-type FGF splice variant (42) and may lack (or have a lower expression level of) other auxiliary proteins as well. When present, other auxiliary proteins could enable multiple CaM molecules to be recruited to an Na_V in an excitable cell.

The schematic models in Figure 9*E* show $Na_V1.2_{CTD}$ with both CaM and FGF12A bound to illustrate how partially ($(Ca^{2+})_2$-CaM_N, apo CaM_C) and fully Ca^{2+}-saturated CaM may recognize the $Na_V1.2$ IQ motif and FGF12A CaMBD and how two CaM molecules might bind. The stoichiometry between CaM, $Na_V1.2_{CTD}$, and FGF12A and locations of CaM reflect those used in the Ca^{2+} titrations of the CaM+FGF12A+-$Na_V1.2_{CTD}$ complex and the results of those experiments (Fig. 6, *E* and *F*, and Fig. 7, *A–E*). However, the finding that $(Ca^{2+})_4$-CaM binds the isolated FGF12A LTP with a weaker affinity than the CaMBD suggests that at a sufficiently high local CaM concentration a third CaM molecule could also bind to the LTP.

Multiple reports have found that $(Ca^{2+})_4$-CaM binds the highly conserved linker between domains III and IV (DIII–DIV linker) (56, 84–87). Recently CaM has also been reported to associate with a site in the NTD of $Na_V1.5$ (88). The direct binding of $(Ca^{2+})_4$-CaM to the LTP and CaMBD in the NTD of the A-type FGFs suggests that, when bound to an A-type FGF, the CTD of an Na_V may associate with three molecules of CaM simultaneously. Thus, in the cell an Na_V with a bound A-type FGF could potentially bind multiple CaM molecules.

Within the context of a cell, multiple targets compete for CaM, making free CaM a limiting reagent in the cytosol (89, 90). However, a number of CaM-binding proteins are found near or within the membrane that may serve as sinks. Among these proteins are ion channels including the Na_V, Ca_V, SK channels, and NMDA receptor, which can form clusters in the membrane (91–93) that would have high local CaM concentrations. Additional CaM-binding targets, such as neurogranin (94, 95) and neuromodulin (96), constitutively bind apo CaM and release it upon Ca^{2+} binding. This may provide a pool of free CaM on the intracellular side of the plasma membrane that could allow recruitment of additional CaM to an Na_V associated with an A-type FGF.

Flux of Na^{2+} through the pore of the Na_V α-subunit is tightly regulated by a network of intramolecular conformational changes and direct interactions with auxiliary proteins that are expressed as different isoforms and splice variants. These may interact with each other as well as with the channel, which could contribute to how they tune Na_V function. An understanding of the structural and energetic forces driving direct interactions between individual auxiliary proteins present at an Na_V will provide valuable insights into how they work in concert to modulate channel function as well as how mutations within their sequences disrupt regulatory processes.

The thermodynamic and structural studies here are the first to identify a direct Ca^{2+}-dependent interaction between CaM and the NTD of A-type FGFs and suggest that Ca^{2+}-saturated CaM may translocate from the Na_V IQ motif to the FGF CaMBD. These findings lay the groundwork for future studies investigating the consequence of the $(Ca^{2+})_4$-CaM–FGF CaMBD interaction on Na_V function.

Experimental procedures

Modeling software and protein structure images

Model structures of human full-length FGF11A (UniProt ID: Q92914), FGF12A (UniProt ID: P61328), FGF13A (UniProt ID: Q92913), and FGF14A (UniProt ID: Q92915) were generated with the Robetta server (https://robetta.bakerlab.org/) (54). Helical wheels of the FGF12A LTP (aa 1–23) and CaMBD (38–64) were made with HeliQuest (https://heliquest.ipmc.cnrs.fr/) (97). PyMOL (Schrödinger LLC) was used to render all protein structures with these color conventions (unless stated otherwise): CaM residue 1–75/blue, 76–80/black, 81–148/red, Ca^{2+}/yellow, Na_V/green, FGF12B/light

gray, FGF12A/deep purple, FGF12A LTP/forest green, and FGF12A CaMBD/limon, and calculate vacuum electrostatic surfaces.

Protein expression and purification

Full-length (aa 1–148) and domain fragments (CaM_N [aa 1–75], CaM_C [aa 76–148]) of WT or mutant human CaM sequences were bacterially overexpressed and purified (23, 98). Genes for full-length or domain fragments of WT or mutant CaM sequences [E31Q/E67Q (E32Q/E68Q) and E104Q/E140Q (E105Q/E141Q)] were expressed with a pT7-7 vector (23). The standard protein designation for each mutant is given first. The parenthetical notation corresponds to the UniProt convention in which the initial Met is designated as residue 1. The three human genes for CaM (CALM1, CALM2, and CALM3) all code for the same protein sequence that corresponds to the sequence of WT CaM used in this study.

The $FGF12A_{CaMBDp}$ (aa 41–70, [CERHVLGVFSK VRFCSGRKRPVRRRPEPQL]), $FGF11A_{NTD}$ (aa 1–68) $FGF12A_{NTD}$ (aa 1–70), $FGF13A_{NTD}$ (aa 1–66), $FGF14A_{NTD}$ (aa 1–68), full-length FGF12A (aa 1–243), full-length FGF12B (aa 1–181), and $Na_V1.2_{CTD}$ (aa 1777–1937) were expressed with an N-terminal His-GST-tag using a pBG101 vector (99). The $FGF12A_{CaMBDp}$, $FGF11A_{NTD}$, $FGF12A_{NTD}$, $FGF13A_{NTD}$, $FGF14A_{NTD}$, FGF12A, FGF12B, and $Na_V1.2_{CTD}$ constructs contained four nonnative residues (GPGS) at the N terminus after removal of the His-GST-tag with 3C protease. FGF12B and complexes of full-length CaM bound to human $FGF12A_{CaMBD}$, $FGF11A_{NTD}$, $FGF12A_{NTD}$, $FGF13A_{NTD}$, $FGF14A_{NTD}$, or human $Na_V1.2_{CTD}$ (SCN2A) were made by bacterial coexpression and purified as previously described (100). Purity was assessed by SDS-PAGE, UV/Vis spectroscopy, and rpHPLC.

Purification and refolding of full-length FGF12A from inclusion bodies

The cell pellet was thawed, resuspended in lysis buffer (50 mM Tris, 500 mM KCl, 0.01% (w/v) NaN_3, 1 mM DTT, 1% (v/v) Triton X-100, pH = 7.4), sonicated, and centrifuged (15,000 rpm, 4 °C, 20 min). The supernatant was discarded, and the pellet was stored at −80 °C. Inclusion bodies were solubilized for 2 h at 22–25 °C, with gentle rocking, in 50 mM Tris, 100 mM KCl, 5 mM imidazole, 6 M guanidine HCl, 1 mM DTT, 0.01% (w/v) NaN_3, pH 7.4. The sample was then centrifuged (25,000 rpm, 4 °C, 25 min), the supernatant passed through a sterile 0.45 μM PVFD filter and loaded onto 5 ml of nickel sepharose resin (GE Life Sciences) equilibrated in wash buffer (50 mM Tris, 100 mM KCl, 20 mM imidazole, 6 M urea, 1 mM DTT, 0.01% (w/v) NaN_3, 1 mM DTT, pH 7.4). The resin was then washed with 25 ml of wash buffer, and the His-GST-tagged FGF12A was eluted with elution buffer (wash buffer with 500 mM imidazole).

Full-length FGF12A was then refolded by rapid dilution into refolding buffer (100 mM Tris, 200 mM KCl, 100 mM L-arginine, 5% (w/v) sucrose, 0.02% NaN_3, 2 mM DTT, pH 7.7, 500 ml per L of cell growth) at 4 °C stirred at 700 rpm with a Teflon-coated stir bar. Prior to the addition of the denaturated His-GST-FGF12A, the CaM+$Na_V1.2_{CTD}$ complex (final concentration 0.2 μM) was added to the refolding buffer to assist FGF12A refolding. Twenty-four hours after the addition of His-GST-FGF12A, insoluble material was removed by centrifugation (20,000 rpm, 4 °C, 20 min) and the sample was concentrated. The HIS-GST-tag was cleaved with 3C protease and removed by repassing the sample over nickel sepharose resin. Anion exchange chromatography (pH 8.5–7.4, KCl 0–300 mM) separated FGF12A and $Na_V1.2_{CTD}$ from CaM to make the FGF12A+$Na_V1.2_{CTD}$ complex. Complex purity (>95%) was assessed by SDS-PAGE, rpHPLC, and UV-Vis spectroscopy.

Affinity of CaM for FGF biosensors

YFP-CFP biosensors containing the sequences for WT human FGF11A CaMBD (aa 36–62), FGF12A LTP (aa 1–23), FGF12A CaMBD (aa 38–64), FGF13A CaMBD (aa 35–60), or FGF14A CaMBD (aa 37–63) were expressed from a pET21B vector (25) (parent vector from A. Persechini and D.J. Black (UMKC) (101, 102)). The FGF sequence used in each biosensor is given in Table 5. Biosensors (≥1 nM) were titrated with WT or mutant CaM (50 mM HEPES, 100 mM KCl, 1 mM $MgCl_2$, 50 μM EGTA, 5 mM NTA, 1.5 μM BSA, 500 μM DTT, 1 mM $CaCl_2$, pH 7.4, 22 °C) in a stirred, water-jacketed quartz cuvette. The steady-state fluorescence intensity of CFP (λ_{EX} 430 nm, λ_{EM} 475 nm), YFP (λ_{EX} 430 nm, λ_{EM} 525 nm), and an experimentally determined isoemissive point (λ_{EX} 430 nm, λ_{EM} 509–513 nm) were monitored throughout the titration with a PTI QM4 fluorimeter (4 nm excitation, 8 nm emission bandpasses, 4–16 s integration). Emission spectra (λ_{EX} 430 nm, 4 nm excitation, 8 nm emission bandpasses, 4 s integration) were collected from 450 to 550 nm.

Buffer subtracted and dilution-corrected titrations were fit to Equation 1, as described (25).

$$\overline{Y} = \frac{K_a[CaM]_{free}}{1 + K_a[CaM]_{free}} \quad (1)$$

where $[CaM]_{free}$ was calculated using Equation 2,

$$[CaM]_{free} = \frac{-b \pm \sqrt{b^2 - 4K_a(-[CaM]_{total})}}{2K_a} \quad (2)$$

b is $(1 + K_a \cdot [biosensor] - K_a \cdot [CaM]_{total})$, and the positive value is taken as $[CaM]_{free}$. The quality of each fit was judged by evaluating the values of the 67% confidence intervals for each parameter, the span and randomness of the residuals, square root of the variance, and the values of the correlation matrix (30). The magnitude of the confidence intervals was typically smaller and within a factor of 2 of the standard deviation of the average determined from the independent replicate titrations. The average ΔG values and standard deviations from three to nine replicate titrations are reported in Tables 1 and 2. Pairwise comparisons were evaluated using the unpaired t-test (GraphPad Prism, StatPlus); all p values were considered to be

very (<0.005) or extremely (<0.0001) statistically significant unless noted otherwise.

Molar ratio of CaM to FGF NTD

The molar ratio of CaM to FGF NTD in the copurified complexes of $(Ca^{2+})_4$-CaM bound to the $FGF11A_{NTD}$, $FGF12A_{NTD}$, $FGF13A_{NTD}$, or $FGF14A_{NTD}$ was analyzed chromatographically with rpHPLC. The complexes were separated with a Supelco C-18 column with a binary solvent system of water (A) and acetonitrile (B), both with 0.1% (v/v) TFA, using the following gradients: 20%–70% B from 1 to 10 min, 70% B from 10 to 14 min, 70%–90% B from 14 to 16 min. The molar ratio between CaM and the $FGF11A_{NTD}$, $FGF12A_{NTD}$, $FGF13A_{NTD}$, or $FGF14A_{NTD}$ was determined by comparing the area of the absorbance peaks at 220 nm for CaM and the FGF NTD construct in rpHPLC chromatograms.

Solution NMR

Spectra were collected at 25 °C on a Bruker Avance II 500 MHz, Varian Unity Inova 600 MHz, or cryoprobe-equipped Bruker Avance NEO 600 MHz spectrometer. Samples were ^{15}N-$(Ca^{2+})_2$-CaM_N (450 μM), ^{15}N-$(Ca^{2+})_2$-CaM_C (300 μM), ^{15}N-$(Ca^{2+})_4$-CaM+^{14}N-$FGF12A_{CaMBDp}$ (330 μM), ^{14}N-$(Ca^{2+})_4$-CaM+^{15}N-$FGF12A_{CaMBDp}$ (450 μM), ^{15}N-$(Ca^{2+})_4$-CaM+^{14}N-$FGF12A_{NTD}$ (290 μM), or ^{14}N-$(Ca^{2+})_4$-CaM+^{15}N-$FGF12A_{NTD}$ (600 μM) in 50 mM HEPES, 100 mM KCl, 1 mM $MgCl_2$, 50 μM EGTA, 5 mM NTA, 0.01% NaN_3, 10 mM $CaCl_2$, ±1 mM DTT, pH 7.4. Spectra were processed with NMRPipe (103) and analyzed with CCPN Analysis (104). SPARTA+ (Shifts Predicted from Analogy in Residue-type and Torsion Angle) (55) was used to predict the position of peaks for residues 41–70 ($FGF12A_{CaMBDp}$) and 1–70 ($FGF12A_{NTD}$) of model 1 in the ensemble of full-length FGF12A generated with Robetta (54).

Steady-state fluorescence excitation and emission spectra

Excitation (λ_{EM} 280 nm, λ_{EX} 240–270 nm or λ_{EM} 320 nm, λ_{EX} 250–310 nm) and emission (λ_{EX} 250 nm, λ_{EM} 270–370 nm or λ_{EX} 277 nm, λ_{EM} 290–370 nm) spectra of $Na_V1.2_{CTD}$ (4 μM) and FGF12B (5 μM) (50 mM HEPES, 100 mM KCl, 1 mM $MgCl_2$, 50 μM EGTA, 5 mM NTA, 500 μM DTT, ± 10 mM $CaCl_2$, pH 7.4, 22 °C) were collected in a stirred, water-jacketed quartz cuvette with a PTI QM4 fluorimeter. Spectra of were collected with 3 (excitation: λ_{EM} 320 nm, λ_{EX} 250–310 nm, emission: λ_{EX} 277 nm, λ_{EM} 290–370 nm) or 5 nm (excitation: λ_{EM} 280 nm, λ_{EX} 240–270 nm, emission: λ_{EX} 250 nm, λ_{EM} 270–370 nm) bandpasses and a 4 s integration time.

Equilibrium Ca^{2+} titrations

Equilibrium Ca^{2+} titrations of full-length WT CaM (4 μM) alone or with the $FGF12A_{CaMBDp}$ (4 μM), $FGF12A_{NTD}$ (4 μM), $Na_V1.2_{CTD}$ (4 μM), FGF12B (5 μM) and $Na_V1.2_{CTD}$ (4 μM), or FGF12A and $Na_V1.2_{CTD}$ (4 μM) in 5 nM Oregon Green or 50 nM XRhod-5F, 50 mM HEPES, 100 mM KCl, 1 mM $MgCl_2$, 50 μM EGTA, 5 mM NTA, 500 μM DTT, pH 7.4, 22 °C were conducted in a water-jacketed quartz cuvette as described (23). Ca^{2+} titrations of the CaM+FGF12A+$Na_V1.2_{CTD}$ complex conducted at a CaM:FGF12A:$Na_V1.2_{CTD}$ ratio of 2:1:1 were conducted with 8 μM CaM and 4 μM FGF12A+$Na_V1.2_{CTD}$ in the same buffer. Steady-state fluorescence intensity of intrinsic CaM fluorophores, Phe (λ_{EX} 250 nm, λ_{EM} 280 nm) and Tyr (λ_{EX} 277 nm, λ_{EM} 320 nm), was monitored with a PTI QM4 fluorimeter. Phe and Tyr-monitored titrations of CaM alone, +$FGF12A_{CaMBDp}$, or +$FGF12A_{NTD}$ were collected with 3 nm bandpasses and a 4 s integration time. Phe-monitored titrations of the CaM+$Na_V1.2_{CTD}$, +FGF12B+$Na_V1.2_{CTD}$ or +FGF12A+$Na_V1.2_{CTD}$ were collected using 5 nm bandpasses and a 16 s integration time, and Tyr-monitored Ca^{2+} titrations of these complexes were collected with 3 nm bandpasses and a 16 s integration time. The free [Ca^{2+}] was calculated from the change in Oregon Green (λ_{EX} 494 nm, λ_{EM} 521 nm, K_d 34.2 μM) or XRhod-5F (λ_{EX} 576 nm, λ_{EM} 603 nm, K_d 1.78 μM) emission intensity (31). The average affinity and standard deviation from three to four replicate titrations are reported in Tables 3 and 4.

Analysis of Ca^{2+}-binding affinity

Each domain of CaM can be considered a two-site macromolecule and the affinities of Ca^{2+} binding to sites I and II or sites III and IV can be fit to a two-site Adair equation (Equation 3) (23)

$$\overline{Y}_{total} = \overline{Y}_2 = \frac{K_1[X]+2K_2[X]^2}{2\left(1+K_1[X]+K_2[X]^2\right)} \quad (3)$$

where K_1 ($\Delta G_1 = -RTlnK_1$) is the sum of the intrinsic constants ($k_1 + k_2$) of the two sites in either domain of CaM, K_2 ($\Delta G_2 = -RTlnK_2$) is the product of the intrinsic constants and the cooperativity constant ($k_1 \cdot k_2 \cdot k_c$), and [X] is the free [Ca^{2+}].

To account for variations in intensity between experiments, the low and high endpoints of each titration were fit to the function *[f(x)]* shown in Equation 4 with nonlinear least squares analysis.

$$f(X) = Y_{[X]low} + \overline{Y}_2 \cdot Span \quad (4)$$

The variable $Y_{[X]low}$ corresponds to the intensity of the Ca^{2+}-depleted sample, $\overline{Y}_2$ is the average fractional saturation, and Span accounts for the difference in intensity at the highest and lowest ligand concentrations. Ca^{2+} titrations of CaM in the presence of the $FGF12A_{CaMBDp}$, $FGF12_{NTD}$, $Na_V1.2_{CTD}$, FGF12B and $Na_V1.2_{CTD}$, or FGF12A and $Na_V1.2_{CTD}$ were analyzed assuming that each domain of CaM contained two functional Ca^{2+}-binding sites. Pairwise comparisons of ΔG determinations were evaluated using the unpaired *t* test (GraphPad Prism, StatPlus); all *p* values were considered to be very (<0.005) or extremely (<0.0001) statistically significant unless noted otherwise.

Analysis of Ca^{2+}-binding affinity of CaM+FGF12A+$Na_V1.2_{CTD}$

Ca^{2+} titrations of CaM sites I and II in the CaM+FGF12A+-$Na_V1.2_{CTD}$ complex conducted at a [CaM]:[FGF12A]:[$Na_V1.2_{CTD}$]

ratio of 2:1:1 were fit to Equation 5. Ca^{2+} titrations of CaM sites III and IV in the same complex were fit to the biphasic function [f(x)] shown in Equation 5 as previously described (37).

$$f(X) = \overline{Y_{2A}} \cdot Span_A + \overline{Y_{2B}} \cdot Span_B + Y_{[X]low} \quad (5)$$

The variables $\overline{Y}_{2A}$ and $\overline{Y}_{2B}$ are the average fractional saturation of the Ca^{2+}-binding sites that correspond to the first and second transitions, respectively. $Span_A$ and $Span_B$ account for the direction and magnitude of signal change in the first and second transitions, respectively, and $Y_{[X]low}$ is the intensity of the Ca^{2+}-depleted sample.

Fractional population of intermediate states

The fractional populations of ligated species shown in Figure 9, *A* and *B* were calculated with a standard Boltzmann distribution, where the probability (f_s) of a species (s) is given by Equation 6:

$$f_s = \frac{\exp(-\Delta G_s/RT)[X]^j}{\sum_{s,j} \exp-\Delta G_s/RT)[X]^j} \quad (6)$$

where [X] is the free [Ca^{2+}], j is the stoichiometry of Ca^{2+} bound by species s, and ΔG_s represents the free energy of species s, which includes the intrinsic binding affinity for each site (k_I and k_{II} for CaM_N, and k_{III} and k_{IV} for CaM_C) and cooperative interactions between the sites ($k_{I\text{-}II}$ or $k_{III\text{-}IV}$). The curves in Figure 9, *A* and *B* were simulated using the ΔG_1 values for Ca^{2+} binding by CaM in the CaM+FGF12B+$Na_V1.2_{CTD}$ or CaM+FGF12A+$Na_V1.2_{CTD}$ complexes reported in Table 4 and assumed that the intrinsic Ca^{2+}-binding affinities of both sites in each domain were equal (*i.e.*, $k_I = k_{II} = k_N$ and $k_{III} = k_{IV} = k_C$), as described previously (23). For CaM in the CaM+FGF12B+$Na_V1.2_{CTD}$ complex k_N and $k_{I\text{-}II}$ were 1.39×10^4 M^{-1} and 284.3, respectively, and k_C and $k_{III\text{-}IV}$ were 5.36×10^3 M^{-1} and 1.5, respectively. For CaM in the CaM+FGF12A+$Na_V1.2_{CTD}$ complex k_N and $k_{I\text{-}II}$ were 1.04×10^5 M^{-1} and 11.9, respectively, and k_C and $k_{III\text{-}IV}$ were 4.30×10^3 M^{-1} and 198.1, respectively.

Modeling of FGF12A and FGF13A CaMBD bound to (Ca^{2+})$_4$-CaM

Models of (Ca^{2+})$_4$-CaM bound to the FGF12 (aa 38–64) and FGF13A (aa 35–60) CaMBD were generated by aligning idealized α-helical models of both FGF CaMBDs to the crystallographic structure of (Ca^{2+})$_4$-CaM bound to the NMDA receptor CaMBD (2HQW.pdb) (68). The α-helical models FGF12A CaMBD and FGF13A CaMBD were aligned to the structure with NMDA receptor CaMBD residues 880–886 in PyMOL (Schrödinger LLC). Coordinates of the initial models were then energy-minimized with YASARA (105) using the default em_runclean macro.

Data availability

Data reported in this publication are shown in the figures and contained within the article or available upon request from the corresponding author (Madeline A. Shea, madeline-shea@uiowa.edu).

Supporting information—This article contains supporting information.

Acknowledgments—We thank Brenda R. Sorensen, Holly M. Isbell, Joseph P. Burba, and Imad Isehak for preliminary studies, Krista Bergquist for technical assistance, and Christopher P. Ptak for NMR support.

Funding and additional information—These studies were supported by the Interdisciplinary Training in Pain Research Program National Institutes of Health T32 NS045549 (R. M.); University of Iowa ICRU Fellowship (C. R. R.); University of Iowa Carver College of Medicine Biochemistry Summer Undergraduate Research Fellowship (M. R. H.); the US National Institutes of Health R01 GM57001 (M. A. S.). The content of this article is solely the responsibility of the authors and does not necessarily represent the official views of the National Institutes of Health.

Author contributions—R. M. and M. A. S. conceptualization; R. M., C. R. R., S. C. H., M. R. H., and M. A. S. investigation; R. M., S. C. H., and M. A. S. formal analysis; R. M., C. R. R., and M. A. S. visualization; R. M. and M. A. S. writing—original draft; R. M., C. R. R., and M. A. S. writing—review and editing; R. M., C. R. R., M. R. H., and M. A. S. funding acquisition.

Conflicts of interest—The authors declare that they have no conflicts of interest with the contents of this article.

Abbreviations—The abbreviations used are: CaM, calmodulin; CaMBD, CaM-binding domain; CTD, C-terminal domain; FGF, fibroblast growth factor homologous factor; Nav, voltage-gated sodium channel; NTD, N-terminal domain.

References

1. Messner, D. J., and Catterall, W. A. (1985) The sodium channel from rat brain. Separation and characterization of subunits. *J. Biol. Chem.* **260**, 10597–10604
2. Fujiwara, T., Sugawara, T., Mazaki-Miyazaki, E., Takahashi, Y., Fukushima, K., Watanabe, M., Hara, K., Morikawa, T., Yagi, K., Yamakawa, K., and Inoue, Y. (2003) Mutations of sodium channel alpha subunit type 1 (SCN1A) in intractable childhood epilepsies with frequent generalized tonic-clonic seizures. *Brain* **126**(Pt 3), 531–546
3. Sugawara, T., Tsurubuchi, Y., Agarwala, K. L., Ito, M., Fukuma, G., Mazaki-Miyazaki, E., Nagafuji, H., Noda, M., Imoto, K., Wada, K., Mitsudome, A., Kaneko, S., Montal, M., Nagata, K., Hirose, S., *et al.* (2001) A missense mutation of the Na^+ channel α_{II} subunit gene $Na_V1.2$ in a patient with febrile and afebrile seizures causes channel dysfunction. *Proc. Natl. Acad. Sci. U. S. A.* **98**, 6384–6389
4. Mantegazza, M., Gambardella, A., Rusconi, R., Schiavon, E., Annesi, F., Cassulini, R. R., Labate, A., Carrideo, S., Chifari, R., Canevini, M. P., Canger, R., Franceschetti, S., Annesi, G., Wanke, E., and Quattrone, A. (2005) Identification of an $Na_V1.1$ sodium channel (SCN1A) loss-of-function mutation associated with familial simple febrile seizures. *Proc. Natl. Acad. Sci. U. S. A.* **102**, 18177–18182
5. Ogiwara, I., Ito, K., Sawaishi, Y., Osaka, H., Mazaki, E., Inoue, I., Montal, M., Hashikawa, T., Shike, T., Fujiwara, T., Inoue, Y., Kaneda, M., and Yamakawa, K. (2009) De novo mutations of voltage-gated sodium channel alphaII gene SCN2A in intractable epilepsies. *Neurology* **73**, 1046–1053

6. Shi, X., Yasumoto, S., Kurahashi, H., Nakagawa, E., Fukasawa, T., Uchiya, S., and Hirose, S. (2012) Clinical spectrum of SCN2A mutations. *Brain Dev.* **34**, 541–545
7. Tester, D. J., Will, M. L., Haglund, C. M., and Ackerman, M. J. (2005) Compendium of cardiac channel mutations in 541 consecutive unrelated patients referred for long QT syndrome genetic testing. *Heart Rhythm* **2**, 507–517
8. Kapplinger, J. D., Tester, D. J., Salisbury, B. A., Carr, J. L., Harris-Kerr, C., Pollevick, G. D., Wilde, A. A., and Ackerman, M. J. (2009) Spectrum and prevalence of mutations from the first 2,500 consecutive unrelated patients referred for the FAMILION long QT syndrome genetic test. *Heart Rhythm* **6**, 1297–1303
9. Bankston, J. R., Yue, M., Chung, W., Spyres, M., Pass, R. H., Silver, E., Sampson, K. J., and Kass, R. S. (2007) A novel and lethal de novo LQT-3 mutation in a newborn with distinct molecular pharmacology and therapeutic response. *PLoS One* **2**, e1258
10. Wang, Q., Shen, J., Splawski, I., Atkinson, D., Li, Z., Robinson, J. L., Moss, A. J., Towbin, J. A., and Keating, M. T. (1995) SCN5A mutations associated with an inherited cardiac arrhythmia, long QT syndrome. *Cell* **80**, 805–811
11. Yang, Y., Wang, Y., Li, S., Xu, Z., Li, H., Ma, L., Fan, J., Bu, D., Liu, B., Fan, Z., Wu, G., Jin, J., Ding, B., Zhu, X., and Shen, Y. (2004) Mutations in SCN9A, encoding a sodium channel alpha subunit, in patients with primary erythermalgia. *J. Med. Genet.* **41**, 171–174
12. Wu, M. T., Huang, P. Y., Yen, C. T., Chen, C. C., and Lee, M. J. (2013) A novel SCN9A mutation responsible for primary erythromelalgia and is resistant to the treatment of sodium channel blockers. *PLoS One* **8**, e55212
13. Faber, C. G., Lauria, G., Merkies, I. S., Cheng, X., Han, C., Ahn, H. S., Persson, A. K., Hoeijmakers, J. G., Gerrits, M. M., Pierro, T., Lombardi, R., Kapetis, D., Dib-Hajj, S. D., and Waxman, S. G. (2012) Gain-of-function Nav1.8 mutations in painful neuropathy. *Proc. Natl. Acad. Sci. U. S. A.* **109**, 19444–19449
14. Vassilev, P. M., Scheuer, T., and Catterall, W. A. (1988) Identification of an intracellular peptide segment involved in sodium channel inactivation. *Science* **241**, 1658–1661
15. Mantegazza, M., Yu, F. H., Catterall, W. A., and Scheuer, T. (2001) Role of the C-terminal domain in inactivation of brain and cardiac sodium channel. *Proc. Natl. Acad. Sci. U. S. A.* **98**, 15348–15353
16. Wildburger, N. C., Ali, S. R., Hsu, W. C., Shavkunov, A. S., Nenov, M. N., Lichti, C. F., LeDuc, R. D., Mostovenko, E., Panova-Elektronova, N. I., Emmett, M. R., Nilsson, C. L., and Laezza, F. (2015) Quantitative proteomics reveals protein-protein interactions with fibroblast growth factor 12 as a component of the voltage-gated sodium channel 1.2 (Na_v1.2) macromolecular complex in Mammalian brain. *Mol. Cell Proteomics* **14**, 1288–1300
17. Liu, C., Dib-Hajj, S. D., and Waxman, S. G. (2001) Fibroblast growth factor homologous factor 1B binds to the C terminus of the tetrodotoxin-resistant sodium channel rNa_V1.9a (NaN). *J. Biol. Chem.* **276**, 18925–18933
18. Liu, C. J., Dib-Hajj, S. D., Renganathan, M., Cummins, T. R., and Waxman, S. G. (2003) Modulation of the cardiac sodium channel Na_V1.5 by fibroblast growth factor homologous factor 1B. *J. Biol. Chem.* **278**, 1029–1036
19. Lou, J. Y., Laezza, F., Gerber, B. R., Xiao, M., Yamada, K. A., Hartmann, H., Craig, A. M., Nerbonne, J. M., and Ornitz, D. M. (2005) Fibroblast growth factor 14 is an intracellular modulator of voltage-gated sodium channels. *J. Physiol.* **569**(Pt 1), 179–193
20. Wang, C., Wang, C., Hoch, E. G., and Pitt, G. S. (2011) Identification of novel interaction sites that determine specificity between fibroblast growth factor homologous factors and voltage-gated sodium channels. *J. Biol. Chem.* **286**, 24253–24263
21. Laezza, F., Lampert, A., Kozel, M. A., Gerber, B. R., Rush, A. M., Nerbonne, J. M., Waxman, S. G., Dib-Hajj, S. D., and Ornitz, D. M. (2009) FGF14 N-terminal splice variants differentially modulate Nav1.2 and Nav1.6-encoded sodium channels. *Mol. Cell Neurosciences* **42**, 90–101
22. Mori, M., Konno, T., Ozawa, T., Murata, M., Imoto, K., and Nagayama, K. (2000) Novel Interaction of the voltage-dependent sodium channel (VDSC) with calmodulin: Does VDSC acquire calmodulin-mediated Ca^{2+}-sensitivity? *Biochemistry* **39**, 1316–1323
23. Theoharis, N. T., Sorensen, B. R., Theisen-Toupal, J., and Shea, M. A. (2008) The neuronal voltage-dependent sodium channel Type II IQ Motif lowers the calcium affinity of the C-domain of calmodulin. *Biochemistry* **47**, 112–123
24. Feldkamp, M. D., Yu, L., and Shea, M. A. (2011) Structural and energetic Determinants of apo calmodulin Binding to the IQ Motif of the Na_v1.2 voltage-dependent sodium channel. *Structure* **19**, 733–747
25. Hovey, L., Fowler, C. A., Mahling, R., Lin, Z., Miller, M. S., Marx, D. C., Yoder, J. B., Kim, E. H., Tefft, K. M., Waite, B. C., Feldkamp, M. D., Yu, L., and Shea, M. A. (2017) Calcium triggers reversal of calmodulin on nested anti-parallel sites in the IQ motif of the neuronal voltage-dependent sodium channel Na_V1.2. *Biophys. Chem.* **224**, 1–19
26. Wang, C., Chung, B. C., Yan, H., Wang, H. G., Lee, S. Y., and Pitt, G. S. (2014) Structural analyses of Ca^{2+}/CaM interaction with Na_V channel C-termini reveal mechanisms of calcium-dependent regulation. *Nat. Commun.* **5**, 4896
27. Yoder, J. B., Ben-Johny, M., Farinelli, F., Srinivasan, L., Shoemaker, S. R., Tomaselli, G. F., Gabelli, S. B., and Amzel, L. M. (2019) Ca(2+)-dependent regulation of sodium channels NaV1.4 and NaV1.5 is controlled by the post-IQ motif. *Nat. Commun.* **10**, 1514
28. Gabelli, S. B., Boto, A., Kuhns, V. H., Bianchet, M. A., Farinelli, F., Aripirala, S., Yoder, J., Jakoncic, J., Tomaselli, G. F., and Amzel, L. M. (2014) Regulation of the Na_V1.5 cytoplasmic domain by calmodulin. *Nat. Commun.* **5**, 5126
29. Klee, C. B., Newton, D. L., Ni, W. C., and Haiech, J. (1986) Regulation of the calcium signal by calmodulin. In: Evered, D., Whelan, J., eds. *Calcium and the Cell*, John Wiley & Sons, Chichester, NY: 162–182
30. Sorensen, B. R., and Shea, M. A. (1998) Interactions between domains of apo calmodulin alter calcium binding and stability. *Biochemistry* **37**, 4244–4253
31. Evans, T. I., and Shea, M. A. (2009) Energetics of calmodulin domain interactions with the calmodulin binding domain of CaMKII. *Proteins* **76**, 47–61
32. Cheung, W. Y. (1970) Cyclic 3',5'-nucleotide phosphodiesterase. Demonstration of an activator. *Biochem. Biophys. Res. Commun.* **38**, 533–538
33. Schulman, H., and Greengard, P. (1978) Stimulation of brain membrane protein phosphorylation by calcium and an endogenous heat-stable protein. *Nature* **271**, 478–479
34. Peterson, B. Z., DeMaria, C. D., and Yue, D. T. (1999) Calmodulin Is the Ca^{2+} Sensor for Ca^{2+}-dependent Inactivation of L-type calcium channels. *Neuron* **22**, 549–558
35. Tzortzopoulos, A., Best, S. L., Kalamida, D., and Török, K. (2004) Ca^{2+}/Calmodulin-dependent activation and inactivation mechanisms of αCaMKII and phospho-Thr_{286}-αCaMKII. *Biochemistry* **43**, 6270–6280
36. Li, Z., Zhang, Y., Hedman, A. C., Ames, J. B., and Sacks, D. B. (2017) Calmodulin lobes facilitate dimerization and activation of estrogen receptor-alpha. *J. Biol. Chem.* **292**, 4614–4622
37. O'Donnell, S. E., Yu, L., Fowler, C. A., and Shea, M. A. (2011) Recognition of beta-calcineurin by the domains of calmodulin: Thermodynamic and structural evidence for distinct roles. *Proteins* **79**, 765–786
38. Smallwood, P. M., Munoz-Sanjuan, I., Tong, P., Macke, J. P., Hendry, S. H., Gilbert, D. J., Copeland, N. G., Jenkins, N. A., and Nathans, J. (1996) Fibroblast growth factor (FGF) homologous factors: New members of the FGF family implicated in nervous system development. *Proc. Natl. Acad. Sci. U. S. A.* **93**, 9850–9857
39. Olsen, S. K., Garbi, M., Zampieri, N., Eliseenkova, A. V., Ornitz, D. M., Goldfarb, M., and Mohammadi, M. (2003) Fibroblast growth factor (FGF) homologous factors share structural but not functional homology with FGFs. *J. Biol. Chem.* **278**, 34226–34236
40. Goetz, R., Dover, K., Laezza, F., Shtraizent, N., Huang, X., Tchetchik, D., Eliseenkova, A. V., Xu, C. F., Neubert, T. A., Ornitz, D. M., Goldfarb, M., and Mohammadi, M. (2009) Crystal structure of a fibroblast growth factor homologous factor (FHF) defines a conserved surface on FHFs for binding and modulation of voltage-gated sodium channels. *J. Biol. Chem.* **284**, 17883–17896

41. Ago, H., Kitagawa, Y., Fujishima, A., Matsuura, Y., and Katsube, Y. (1991) Crystal structure of basic fibroblast growth factor at 1.6 A resolution. *J. Biochem.* **110**, 360–363
42. Munoz-Sanjuan, I., Smallwood, P. M., and Nathans, J. (2000) Isoform diversity among fibroblast growth factor homologous factors is generated by alternative promoter usage and differential splicing. *J. Biol. Chem.* **275**, 2589–2597
43. Dover, K., Solinas, S., D'Angelo, E., and Goldfarb, M. (2010) Long-term inactivation particle for voltage-gated sodium channels. *J. Physiol.* **588**(Pt 19), 3695–3711
44. Abrams, J., Roybal, D., Chakouri, N., Katchman, A. N., Weinberg, R., Yang, L., Chen, B. X., Zakharov, S. I., Hennessey, J. A., Avula, U. M. R., Diaz, J., Wang, C., Wan, E. Y., Pitt, G. S., Ben-Johny, M., *et al.* (2020) Fibroblast growth factor homologous factors tune arrhythmogenic late NaV1.5 current in calmodulin binding-deficient channels. *JCI Insight* **5**
45. Hartung, H., Feldman, B., Lovec, H., Coulier, F., Birnbaum, D., and Goldfarb, M. (1997) Murine FGF-12 and FGF-13: Expression in embryonic nervous system, connective tissue and heart. *Mech. Dev.* **64**, 31–39
46. Yang, J., Wang, Z., Sinden, D. S., Wang, X., Shan, B., Yu, X., Zhang, H., Pitt, G. S., and Wang, C. (2016) FGF13 modulates the gating properties of the cardiac sodium channel Nav1.5 in an isoform-specific manner. *Channels (Austin)* **10**, 410–420
47. Effraim, P. R., Huang, J., Lampert, A., Stamboulian, S., Zhao, P., Black, J. A., Dib-Hajj, S. D., and Waxman, S. G. (2019) Fibroblast growth factor homologous factor 2 (FGF-13) associates with Nav1.7 in DRG neurons and alters its current properties in an isoform-dependent manner. *Neurobiol. Pain* **6**, 100029
48. Bosch, M. K., Nerbonne, J. M., Townsend, R. R., Miyazaki, H., Nukina, N., Ornitz, D. M., and Marionneau, C. (2016) Proteomic analysis of native cerebellar iFGF14 complexes. *Channels (Austin)* **10**, 297–312
49. Xiao, M., Bosch, M. K., Nerbonne, J. M., and Ornitz, D. M. (2013) FGF14 localization and organization of the axon initial segment. *Mol. Cell Neurosciences* **56**, 393–403
50. Ben-Johny, M., Yue, D. N., and Yue, D. T. (2016) Detecting stoichiometry of macromolecular complexes in live cells using FRET. *Nat. Commun.* **7**, 13709
51. Wang, C., Chung, B. C., Yan, H., Lee, S. Y., and Pitt, G. S. (2012) Crystal Structure of the ternary Complex of a NaV C-terminal domain, a fibroblast growth factor homologous factor, and calmodulin. *Structure* **20**, 1167–1176
52. Niu, J., Dick, I. E., Yang, W., Bamgboye, M. A., Yue, D. T., Tomaselli, G., Inoue, T., and Ben-Johny, M. (2018) Allosteric regulators selectively prevent Ca^{2+}-feedback of Ca_V and Na_V channels. *Elife* **7**, e35222
53. Ishida, T., and Kinoshita, K. (2008) Prediction of disordered regions in proteins based on the meta approach. *Bioinformatics* **24**, 1344–1348
54. Kim, D. E., Chivian, D., and Baker, D. (2004) Protein structure prediction and analysis using the Robetta server. *Nucleic Acids Res.* **32**, W526–W531
55. Shen, Y., and Bax, A. (2010) SPARTA+: A modest improvement in empirical NMR chemical shift prediction by means of an artificial neural network. *J. Biomol. NMR* **48**, 13–22
56. Shah, V. N., Wingo, T. L., Weiss, K. L., Williams, C. K., Balser, J. R., and Chazin, W. J. (2006) Calcium-dependent regulation of the voltage-gated sodium channel hH1: Intrinsic and extrinsic sensors use a common molecular switch. *Proc. Natl. Acad. Sci. U. S. A.* **103**, 3592–3597
57. Sorensen, B. R., Faga, L. A., Hultman, R., and Shea, M. A. (2002) Interdomain linker increases thermostability and decreases calcium affinity of calmodulin N-domain. *Biochemistry* **41**, 15–20
58. Pablo, J. L., and Pitt, G. S. (2017) FGF14 is a regulator of KCNQ2/3 channels. *Proc. Natl. Acad. Sci. U. S. A.* **114**, 154–159
59. Schoorlemmer, J., and Goldfarb, M. (2001) Fibroblast growth factor homologous factors are intracellular signaling proteins. *Curr. Biol.* **11**, 793–797
60. Schulman, H., Hanson, P. I., and Meyer, T. (1992) Decoding calcium signals by multifunctional CaM kinase. *Cell Calcium* **13**, 401–411
61. Hathaway, D. R., Adelstein, R. S., and Klee, C. B. (1981) Interaction of calmodulin with myosin light chain kinase and cAMP-dependent protein kinase in bovine brain. *J. Biol. Chem.* **256**, 8183–8189
62. Hubbard, M. J., and Klee, C. B. (1987) Calmodulin binding by calcineurin ligand-induced renaturation of protein immobilized on nitrocellulose. *J.Biol.Chem.* **262**, 15062–15070
63. Chen, Y., Clarke, O. B., Kim, J., Stowe, S., Kim, Y.-K., Assur, Z., Cavalier, M., Godoy-Ruiz, R., von Alpen, D. C., Manzini, C., Blaner, W. S., Frank, J., Quadro, L., Weber, D. J., Shapiro, L., *et al.* (2016) Structure of the STRA6 receptor for retinol uptake. *Science* **353**, aad8266
64. Lee, C. H., and MacKinnon, R. (2018) Activation mechanism of a human SK-calmodulin channel complex elucidated by cryo-EM structures. *Science* **360**, 508–513
65. Houdusse, A., Gaucher, J. F., Krementsova, E., Mui, S., Trybus, K. M., and Cohen, C. (2006) Crystal structure of apo-calmodulin bound to the first two IQ motifs of myosin V reveals essential recognition features. *Proc. Natl. Acad. Sci. U. S. A.* **103**, 19326–19331
66. Meador, W. E., Means, A. R., and Quiocho, F. A. (1992) Target enzyme recognition by calmodulin: 2.4 Å Structure of a calmodulin-peptide complex. *Science* **257**, 1251–1255
67. Ehlers, M. D., Zhang, S., Bernhardt, J. P., and Huganir, R. L. (1996) Inactivation of NMDA receptors by direct interaction of calmodulin with the NR1 subunit. *Cell* **84**, 745–755
68. Ataman, Z. A., Gakhar, L., Sorensen, B. R., Hell, J. W., and Shea, M. A. (2007) The NMDA receptor NR1 C1 region bound to calmodulin: Structural insights into functional differences between homologous domains. *Structure* **15**, 1603–1617
69. Newman, R. A., Van Scyoc, W. S., Sorensen, B. R., Jaren, O. R., and Shea, M. A. (2008) Interdomain cooperativity of calmodulin bound to melittin preferentially increases calcium affinity of sites I and II. *Proteins* **71**, 1792–1812
70. van Petegem, F., Chatelain, F. C., and Minor, D. L., Jr. (2005) Insights into voltage-gated calcium channel regulation from the structure of the $Ca_{(V)}$1.2 IQ domain-Ca^{2+}/calmodulin complex. *Nat. Struct. Mol. Biol.* **12**, 1108–1115
71. Kim, E. Y., Rumpf, C. H., Fujiwara, Y., Cooley, E. S., Van Petegem, F., and Minor, D. L., Jr. (2008) Structures of Ca_V2 Ca^{2+}/CaM-IQ domain complexes reveal binding modes that underlie calcium-dependent inactivation and facilitation. *Structure* **16**, 1455–1467
72. Osawa, M., Tokumitsu, H., Swindells, M. B., Kurihara, H., Orita, M., Shibanuma, T., Furuya, T., and Ikura, M. (1999) A novel target recognition revealed by calmodulin in complex with Ca^{2+}-calmodulin-dependent kinase kinase. *Nat. Struct. Biol.* **6**, 819–824
73. Mori, M. X., Vander Kooi, C. W., Leahy, D. J., and Yue, D. T. (2008) Crystal structure of the Ca_V2 IQ domain in complex with Ca^{2+}/calmodulin: High-resolution mechanistic implications for channel regulation by Ca^{2+}. *Structure* **16**, 607–620
74. Feldkamp, M. D., Gakhar, L., Pandey, N., and Shea, M. A. (2015) Opposing orientations of the anti-psychotic drug trifluoperazine selected by alternate conformations of M144 in calmodulin. *Proteins* **83**, 989–996
75. Vertessy, B. G., Harmat, V., Bocskei, Z., Naray-Szabo, G., Orosz, F., and Ovadi, J. (1998) Simultaneous binding of drugs with different chemical structures to Ca2+-calmodulin: Crystallographic and spectroscopic studies. *Biochemistry* **37**, 15300–15310
76. Cook, W. J., Walter, L. J., and Walter, M. R. (1994) Drug binding by calmodulin: Crystal structure of a calmodulin-trifluoperazine complex. *Biochemistry* **33**, 15259–15265
77. Li, R., Leblanc, J., He, K., and Liu, X. J. (2016) Spindle function in Xenopus oocytes involves possible nanodomain calcium signaling. *Mol. Biol. Cell* **27**, 3273–3283
78. Wang, C., Hennessey, J. A., Kirkton, R. D., Wang, C., Graham, V., Puranam, R. S., Rosenberg, P. B., Bursac, N., and Pitt, G. S. (2011) Fibroblast growth factor homologous factor 13 regulates Na+ channels and conduction velocity in murine hearts. *Circ. Res.* **109**, 775–782
79. Pablo, J. L., Wang, C., Presby, M. M., and Pitt, G. S. (2016) Polarized localization of voltage-gated Na+ channels is regulated by concerted FGF13 and FGF14 action. *Proc. Natl. Acad. Sci. U. S. A.* **113**, E2665–E2674

80. Biswas, S., Deschenes, I., Disilvestre, D., Tian, Y., Halperin, V. L., and Tomaselli, G. F. (2008) Calmodulin regulation of $Na_V1.4$ current: Role of binding to the carboxyl terminus. *J. Gen. Physiol.* **131**, 197–209
81. Schaller, K. L., and Caldwell, J. H. (2003) Expression and distribution of voltage-gated sodium channels in the cerebellum. *Cerebellum* **2**, 2–9
82. Whitaker, W. R., Clare, J. J., Powell, A. J., Chen, Y. H., Faull, R. L., and Emson, P. C. (2000) Distribution of voltage-gated sodium channel alpha-subunit and beta-subunit mRNAs in human hippocampal formation, cortex, and cerebellum. *J. Comp. Neurol.* **422**, 123–139
83. Kim, E. Y., Rumpf, C. H., Van Petegem, F., Arant, R. J., Findeisen, F., Cooley, E. S., Isacoff, E. Y., and Minor, D. L., Jr. (2010) Multiple C-terminal tail Ca^{2+}/CaMs regulate $Ca_V1.2$ function but do not mediate channel dimerization. *EMBO J.* **29**, 3924–3938
84. Potet, F., Chagot, B., Anghelescu, M., Viswanathan, P. C., Stepanovic, S. Z., Kupershmidt, S., Chazin, W. J., and Balser, J. R. (2009) Functional interactions between distinct sodium channel cytoplasmic domains through the action of calmodulin. *J. Biol. Chem.* **284**, 8846–8854
85. Sarhan, M. F., Van Petegem, F., and Ahern, C. A. (2009) A double tyrosine motif in the cardiac sodium channel domain III-IV linker couples calcium-dependent calmodulin binding to inactivation gating. *J. Biol. Chem.* **284**, 33265–33274
86. Sarhan, M. F., Tung, C. C., Van Petegem, F., and Ahern, C. A. (2012) Crystallographic basis for calcium regulation of sodium channels. *Proc. Natl. Acad. Sci. U. S. A.* **109**, 3558–3563
87. Johnson, C. N., Potet, F., Thompson, M. K., Kroncke, B. M., Glazer, A. M., Voehler, M. W., Knollmann, B. C., George, A. L., Jr., and Chazin, W. J. (2018) A mechanism of calmodulin modulation of the human cardiac sodium channel. *Structure* **26**, 683–694 e3
88. Wang, Z., Vermij, S. H., Sottas, V., Shestak, A., Ross-Kaschitza, D., Zaklyazminskaya, E. V., Hudmon, A., Pitt, G. S., Rougier, J. S., and Abriel, H. (2020) Calmodulin binds to the N-terminal domain of the cardiac sodium channel Nav1.5. *Channels (Austin)* **14**, 268–286
89. Persechini, A., and Cronk, B. (1999) The Relationship between the free Concentrations of Ca^{2+} and Ca^{2+}-calmodulin in intact cells. *J. Biol. Chem.* **274**, 6827–6830
90. Maier, L. S., Ziolo, M. T., Bossuyt, J., Persechini, A., Mestril, R., and Bers, D. M. (2006) Dynamic changes in free Ca-calmodulin levels in adult cardiac myocytes. *J. Mol. Cell Cardiol.* **41**, 451–458
91. Westenbroek, R. E., Merrick, D. K., and Catterall, W. A. (1989) Differential subcellular localization of the R_I and R_{II} Na^+ channel subtypes in central neurons. *Neuron* **3**, 695–704
92. Clatot, J., Hoshi, M., Wan, X., Liu, H., Jain, A., Shinlapawittayatorn, K., Marionneau, C., Ficker, E., Ha, T., and Deschenes, I. (2017) Voltage-gated sodium channels assemble and gate as dimers. *Nat. Commun.* **8**, 2077
93. Zhou, D., Lambert, S., Malen, P. L., Carpenter, S., Boland, L. M., and Bennett, V. (1998) $Ankyrin_G$ is required for clustering of voltage-gated Na channels at axon initial segments and for normal action potential firing. *J. Cell Biol.* **143**, 1295–1304
94. Gerendasy, D. D., Herron, S. R., Watson, J. B., and Sutcliffe, J. G. (1994) Mutational and biophysical studies suggest RC3/neurogranin regulates calmodulin availability. *J. Biol. Chem.* **269**, 22420–22426
95. Gerendasy, D. D., Herron, S. R., Jennings, P. A., and Sutcliffe, J. G. (1995) Calmodulin stabilizes an amphiphilic a-helix within RC3/neurogranin and GAP-43/neuromodulin only when Ca^{2+} is absent. *J. Biol. Chem.* **270**, 6741–6750
96. Chapman, E. R., Au, D., Alexander, K. A., Nicolson, T. A., and Storm, D. R. (1991) Characterization of the calmodulin binding domain of neuromodulin. Functional significance of serine 41 and phenylalanine 42. *J. Biol. Chem.* **266**, 207–213
97. Gautier, R., Douguet, D., Antonny, B., and Drin, G. (2008) HELIQUEST: A web server to screen sequences with specific alpha-helical properties. *Bioinformatics* **24**, 2101–2102
98. Putkey, J. A., Slaughter, G. R., and Means, A. R. (1985) Bacterial expression and characterization of proteins derived from the chicken calmodulin cDNA and a calmodulin processed gene. *J. Biol. Chem.* **260**, 4704–4712
99. Damo, S. M., Feldkamp, M. D., Chagot, B., and Chazin, W. J. (2013) NMR studies of the interaction of calmodulin with IQ motif peptides. *Methods Mol. Biol.* **963**, 173–186
100. Mahling, R., Kilpatrick, A. M., and Shea, M. A. (2017) Backbone resonance assignments of complexes of human voltage-dependent sodium channel $Na_V1.2$ IQ motif peptide bound to apo calmodulin and to the C-domain fragment of apo calmodulin. *Biomol. NMR Assign.* **11**, 297–303
101. Romoser, V. A., Hinkle, P. M., and Persechini, A. (1997) Detection in living cells of Ca^{2+}-dependent changes in the fluorescence emission of an indicator composed of two green fluorescent protein variants linked by a calmodulin-binding sequence. A new class of fluorescent indicators. *J. Biol. Chem.* **272**, 13270–13274
102. Black, D. J., Leonard, J., and Persechini, A. (2006) Biphasic Ca^{2+}-dependent switching in a calmodulin-IQ domain complex. *Biochemistry* **45**, 6987–6995
103. Delaglio, F., Grzesiek, S., Vuister, G. W., Zhu, G., Pfeifer, J., and Bax, A. (1995) NMRPipe: A multidimensional spectral processing system based on UNIX pipes. *J. Biomol. NMR.* **6**, 277–293
104. Vranken, W. F., Boucher, W., Stevens, T. J., Fogh, R. H., Pajon, A., Llinas, M., Ulrich, E. L., Markley, J. L., Ionides, J., and Laue, E. D. (2005) The CCPN data model for NMR spectroscopy: Development of a software pipeline. *Proteins* **59**, 687–696
105. Krieger, E., and Vriend, G. (2015) New ways to boost molecular dynamics simulations. *J. Comput. Chem.* **36**, 996–1007
106. Apweiler, R., Bairoch, A., Wu, C. H., Barker, W. C., Boeckmann, B., Ferro, S., Gasteiger, E., Huang, H., Lopez, R., Magrane, M., Martin, M. J., Natale, D. A., O'Donovan, C., Redaschi, N., and Yeh, L. S. (2004) UniProt: The universal protein knowledgebase. *Nucleic Acids Res.* **32**, D115–D119
107. Gasteiger, E., Gattiker, A., Hoogland, C., Ivanyi, I., Appel, R. D., and Bairoch, A. (2003) ExPASy: The proteomics server for in-depth protein knowledge and analysis. *Nucleic Acids Res.* **31**, 3784–3788
108. Papadopoulos, J. S., and Agarwala, R. (2007) Cobalt: Constraint-based alignment tool for multiple protein sequences. *Bioinformatics* **23**, 1073–1079

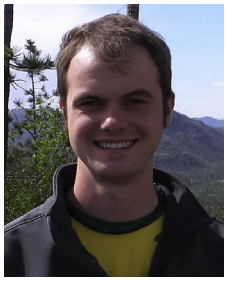

Ryan Mahling conducted this research as a Biochemistry Ph.D. student at the University of Iowa. Focusing on regulation of Na_Vs by multiple auxiliary proteins, he and undergraduate coworkers determined that calmodulin and intracellular FGFs (11A, 12A, 13A, 14A) interact with high affinity, forming a ternary complex with an $Na_V1.2$ fragment. This suggests a new molecular mechanism of allosteric regulation. He will continue this work as a postdoctoral fellow at Columbia University.